Diffuse Auroral Precipitation Effects on Ionospheric Conductance During Magnetic Storms: Comparison of Simulated and Incoherent Radar Scatter-Inferred Conductance

Margaret W. Chen[1], Colby Lemon[1], James Hecht[1], George V. Khazanov[2], J. Scott Evans[3], Stephen Kaeppler[4], Christine Gabrielse[1], and Shun-Rong Zhang[5]

[1]The Aerospace Corporation, El Segundo, CA

[2]NASA Goddard Space Flight Center, Greenbelt, MD

[3]Computational Physics, Inc., Springfield, VA

[4]Clemson University, Clemson, SC

[5]MIT Haystack Observatory

Corresponding author: Margaret Chen (Margaret.W.Chen@aero.org)

Key Points

- Effects of diffuse electron precipitation on Pedersen and Hall conductance and conductivity are simulated for two major geomagnetic storms
- Simulated ionospheric conductance agrees well with conductance inferred from incoherent scatter radar data when there is diffuse aurora
- Simulated storm-time electric intensity followed general trends of measured electric intensity from Poker Flat when there is diffuse aurora

Abstract

We investigated the effects of storm-time diffuse auroral electron precipitation on ionospheric Pedersen and Hall conductivity and conductance during the CME-driven St. Patrick's Day storms of 2013 (min *Dst* = –131 nT) and 2015 (min *Dst* = –233 nT). These storms were simulated using the magnetically and electrically self-consistent RCM-E model with STET modifications, alongside the B3C auroral transport code to compute ionospheric conductivities and height-integrated conductance. The simulation results were validated against conductance inferred from Poker Flat Incoherent Scatter Radar (PFISR) and Millstone Hill Incoherent Scatter Radar (MHISR) measurements. Our simulations show that the magnetic latitude and local time distribution of Pedersen and Hall auroral conductance correlates strongly with diffuse electron precipitation flux, with the plasmapause marking the low-latitude boundary of conductance. Simulated Pedersen/Hall conductance agrees reasonably well with PFISR measurements at 65.9° MLAT during diffuse auroral precipitation. During the intense 2015 storm, diffuse aurora extended down to 52.5° MLAT, with simulated conductance agreeing within a factor of two with MHISR observations. Discrete auroral arcs observed during both storms enhanced PFISR conductance by tens of siemens, though these enhancements were not captured by the model. Additionally, the simulated electric intensity showed development of sub-auroral polarization streams (SAPS) and dawn SAPS features and followed the general trend of Poker Flat electric intensity at 65.9° MLAT during diffuse aurora, despite being updated every 5 minutes. The overall agreement between simulated ionospheric conductance and electric intensity with observations highlights the model's capability during diffuse auroral precipitation.

1 Introduction

Quantifying ionospheric conductance on a global scale has been challenging because direct determination of Hall and Pedersen conductance requires measurements of electron density altitude profiles (e.g., Kosch et al., 1998). Ground-based incoherent scatter radars (ISRs) can provide direct single-point conductivity profile measurements (Brekke et al., 1974) with an assumed neutral composition model. However, they provide very limited spatial coverage since there are a small number of ISRs.

Because electron precipitation can significantly alter ionospheric conductivity and conductance during magnetic disturbances, auroral ionospheric conductance is often inferred from measurements of electron precipitating particle flux. The Robinson et al., (1987) relations or transport codes (e.g., Solomon, 1993; Strickland et al., 1993) are often utilized in these calculations. In-situ measurements such as from DMSP and NOAA satellites provide energy spectral distributions with improved latitudinal coverage compared to ISR data across the auroral oval but with limited local time. On the other hand, auroral imagers such as Polar/UVI (Torr et al., 1995), IMAGE/FUV (Mende et al., 2000), and TIMED/GUVI (Paxton et al., 1999) offer global or regional coverage, but typically assume Maxwellian distributions which can be an oversimplification of the actual distributions. Various statistical conductance models have been developed from in-situ and/or imaging data: Wallis & Budzinski (1981) from Isis-2 data, D. A. Hardy et al. (1985); David A. Hardy et al. (1989) from DMSP data, Fuller-Rowell & Evans (1987) from NOAA-TIROS data, Zhang & Paxton (2008) from GUVI data, P. T. Newell et al. (2014); Patrick T. Newell et al. (2010) OVATION models from DMSP and GUVI data, and McGranaghan et al. (2015, 2016) from DMSP data and GLOW transport model results (Solomon, 1993) with no assumption of Maxwellian distributions of the precipitating electron energy fluxes. In addition, the Assimilative Mapping of Ionospheric Electrodynamics (AMIE) (Lu, 2013; Richmond & Kamide, 1988) can fit input from statistical models of precipitating electron flux and satellite, radar, and ground-based magnetometer observations to produce global maps of high latitude ionospheric conductance. More recently, ionospheric conductivities inferred from Poker Flat ISR measurements and field-aligned currents (FAC) from the Active Magnetosphere and Planetary Electrodynamics Response Experiment (AMPERE) (Robinson et al., 2020) and Swarm (Wang & Zou, 2022) have been correlated and may provide another method for estimating ionospheric conductance at high latitudes.

Empirical models have been employed for calculating auroral electron conductance in several global and inner magnetospheric simulation models. Fits to ISR data were used in the Coupled Magnetosphere Ionosphere Thermosphere (CMIT) model of Wiltberger et al. (2004) that combined the Lyon-Fedder-Mobarry global magnetohydrodynamic (MHD) and Thermosphere

Ionosphere Nested Grid (TING) models. The Comprehensive Ring Current Model (CRCM) (Ebihara, 2004; Ebihara & Fok, 2004; Zheng et al., 2008) utilized the D. A. Hardy et al. (1987) *Kp*-dependent model of conductivities. The combined UCLA MHD and NOAA Coupled Thermosphere Ionosphere Model (CTIM) (Raeder et al., 2013) used conductance calculated from CTIM (Robinson et al., 1987) with statistical models of auroral precipitation based on NOAA-TIROS auroral particle measurements (Fuller-Rowell & Evans, 1987). Particle precipitation in the University of Michigan MHD code depended on simulated field aligned currents (FAC) with a relationship based on analyzing ~8500 ionospheric conductance and FAC patterns from AMIE (Ridley et al., 2001).

Alternative methodologies employed for calculating auroral electron conductance in kinetic inner magnetospheric simulation models include using simulated precipitating electron flux distributions as input to the Robinson et al. (1987) relations (Chen et al., 2019; Chen, Lemon, Guild, et al., 2015; Chen, Lemon, Orlova, et al., 2015; Perlongo et al., 2017; Sazykin et al., 2005) or as input to the Solomon (2001) or Strickland et al. (1993) auroral transport codes (Yu et al., 2018). In these approaches, the auroral conductance is calculated in a manner that is internally consistent with the simulated electric fields, particle transport and precipitation in the inner magnetospheric models. There are also coupled global MHD, kinetic inner magnetospheric, and ionosphere-thermosphere models such as the LFM-TIEGCM-RCM (LTR) model (Liu et al., 2023) in which the conductance is computed. The kinetic inner magnetospheric models have focused on simulating diffuse auroral precipitation, which provides the bulk of the precipitating energy flux into the ionosphere during low and high solar wind driving conditions (Newell, Sotirelis, & Wing, 2009).

Diffuse auroral electron precipitation is caused by pitch-angle scattering of plasma sheet and inner magnetospheric electrons by plasma waves into the loss cone. Whistler chorus waves can effectively pitch-angle scatter electrons from the plasmapause to ~8 R_E (Ni, Thorne, Meredith, et al., 2011; Thorne, 2010) on the pre-midnight to morning side. However, at $L > 8$ where whistler chorus wave intensities are weak, electron cyclotron harmonic (ECH) waves may play a significant role in electron scattering (Ni, Thorne, Liang, et al., 2011).

These electrons scattered into the loss cone, initially transported downward from either hemisphere into the ionosphere and atmosphere, are referred here as the "primary" precipitating electron energy flux. The direction of the "primary" precipitating electron energy flux is illustrated by thick orange arrows in Figure 1 showing a meridional view of the Earth's ionosphere and magnetosphere. The primary precipitated electrons undergo an energy cascade to lower energies within the atmosphere and generate secondary electrons, as indicated by the blue arrows in Figure 1, through impact ionization with neutrals. Khazanov et al. (2017) utilizing the Super Thermal Electron Transport (STET) model has shown that some of the primary electrons are backscattered along magnetic field lines back into the magnetosphere and transported to the conjugate hemisphere, as illustrated by the narrow orange arrows in Figure 1.

Through multiple precipitation, backscattering and magnetospheric interactions, the precipitating electron flux at the upper ionospheric boundary of 700–800 km is amplified compared to the primary precipitating electron flux. Comparisons between the STET model and DMSP (Newell et al., 2009) precipitating electron flux spectra indicate that the multiple reflections effect can account for higher fluxes at energies below ~a few keV than from Maxwellian or Kappa distributions (Wing, Khazanov, et al., 2019). Observed precipitating spectra naturally include multiple reflection magnetosphere-ionosphere (M-I) coupling effects. However, kinetic inner magnetospheric models that simulate only the primary precipitating electron fluxes would need to quantify atmospheric backscatter effects of precipitating electron fluxes (Khazanov & Chen, 2021).

When incorporating STET modifications to account for multiple precipitation and backscattering of the primary electron precipitating fluxes simulated with the magnetically and electrically self-consistent Rice Convection Model – Equilibrium (RCM-E) for the 17 March 2013 storm, Khazanov, Chen, et al. (2019) found significant differences in the global electron precipitating flux and conductance pattern compared to without the STET modifications. With the STET modifications the simulated electric field was weakened where the simulated auroral conductance was augmented early in the storm main phase. Since currents are more easily driven through the ionosphere where the conductance is enhanced, this resulted in less feedback to the electric field or less electric field shielding at lower magnetic latitudes (MLATs) or equatorial geocentric distances r in the auroral region. In this region, with a less shielded electric field on the nightside at lower r values, the ion pressure and associated ring current perturbation magnetic field were larger.

The effects of diffuse auroral electron precipitation on ionospheric conductance are complex as the electrodynamics in the magnetosphere-ionosphere are highly coupled. The ionospheric conductance and field-aligned currents alter the inner magnetospheric electric field that influences inner magnetospheric particle transport, ring current formation, particle precipitation, and field-aligned currents. Using RCM-E simulations with STET modifications and the B3C auroral transport code, we examine the effects of storm-time diffuse auroral electron precipitation on ionospheric Hall and Pedersen conductivity and conductance for two major storms: 17 March 2013 (min Dst = –131 nT) and 17 March 2015 (min Dst = –233 nT). We compare simulated Hall and

Pedersen conductance and electric intensity with corresponding Poker Flat Incoherent Scatter Radar (PFISR) observations during the two events. For the larger 17 March 2015 storm with aurora occurring at low latitudes we compare simulated conductance and conductivity profiles with Millstone Hill (MH) Incoherent Scatter Radar as well. This data-model validation is an important step toward improving global models of ionospheric auroral conductance.

2 RCME-STET-B3C Simulation Model

The block diagram in Figure 1 provides an overview of the electrodynamics of the RCME-STET-B3C simulation model. The RCM-E (Lemon, 2003; Lemon et al., 2004; Toffoletto, 2020) merges the Rice Convection Model (RCM) (Harel et al., 1981; Toffoletto, 2020; Toffoletto et al., 2003) with a time-varying magnetospheric magnetic field that is in force equilibrium with the plasma. The Aerospace version of the RCM-E (Chen et al., 2019; Chen, Lemon, Orlova, et al., 2015) includes the capability to model magnetospheric compressions and expansions (Chen et al., 2012) in the magnetic field solver that led to better agreement between RCM-E and observed magnetic intensities in the inner magnetosphere during a storm event. The magnetic field outer boundary conditions (BC) are specified by TS04 (Tsyganenko & Sitnov, 2005) driven by upstream observational data every 5 minutes obtained from the NASA OMNIWeb (https://omniweb.gsfc.nasa.gov/). The RCM modeling region is within the closed magnetic field (**B**) line region of the inner magnetosphere. The inner RCM radial boundary R_i is at 1.04 R_E and maps to a magnetic latitude of 9°. The outer RCM boundary maps in the equatorial plane to a circle of radius R_b except where it is limited by the magnetopause that expands and contracts in response to solar wind pressure variations. In this study R_b is set at 10 R_E corresponding to a quiet time high magnetic latitude boundary of 67.5° at midnight. During magnetically disturbed times, the RCM high latitude boundary at midnight typically occurs at a magnetic latitude below 67.5°, sometimes

60° or lower, since these magnetic field lines map to an equatorial distance beyond 10 R_E. The RCM has a stationary ionospheric grid in magnetic longitude and latitude with a uniform longitudinal resolution of 2.4°. The stationary ionospheric grid points are unevenly spaced in magnetic latitude to achieve finer spatial resolution in the auroral region. The resolution of the latitudinal grid is a uniform 0.14° from the high latitude boundary down to 54°. Between latitudes of 54° and 9°, the latitudinal grid gradually gets coarser to a maximum spacing of 3.7°.

The RCM computes the bounced-averaged guiding-center drifts of isotropic protons, O^+ ions, and electrons (see the "Particle Drift Currents" box in Figure 1) that are influenced by **B** and $\mathcal{E}$, the electric field. Field-aligned currents (FACs) are calculated from the divergence of particle drift currents to maintain continuity with the currents into and out of the ionosphere. Losses for protons and O^+ ions due to charge exchange with the neutral H exosphere, and precipitation due to field-line curvature (FLC) scattering are taken account of. We use an ion FLC lifetime that is parameterized by the ratio of the ion gyro-radius to the radius of magnetic field curvature and the strong ion diffusion lifetime described by Equation 5 of Chen et al. (2019). The electron loss model includes the effect of scattering due to statistical observations of wave properties with magnetic activity (see the "Wave Scattering Model" box in Figure 1). The RCM-E primary precipitating flux of electrons, the dominant contributor to the particle precipitation into the ionosphere, is modified by results from the STET model that account for backscatter effects. Section 2.1 below explains the diffuse auroral electron precipitation model in detail. The STET-modified electron flux distributions at 500 km are the upper boundary input to the B3C auroral transport model (see "B3C" box in Figure 1). The B3C model calculates profiles of electron density, changes in electron energy flux, and Hall and Pedersen auroral conductivity over altitudes of 90 km to 500 km. The auroral conductance Σ are obtained from integrating the conductivity profiles. The ionospheric conductance model is described in detail in Section 2.2 below. The FACs, ionospheric conductance and ionospheric electric field are related by the current continuity equation ($\nabla \cdot \boldsymbol{J} = 0$), and Ohm's Law ($J_z = \nabla_{x,y} \cdot (\Sigma \cdot \mathcal{E}_{x,y})$). The self-consistent ionospheric electric potentials are calculated every 1 s and are mapped along magnetic field lines using the electrostatic condition ($\mathcal{E} \cdot \boldsymbol{B} = 0$). The electrostatic condition is valid for diffuse auroral precipitation. Discrete aurora precipitation associated with parallel electric fields along closed magnetic field lines is not currently modeled in the RCM-E.

The time dependent electric potential at the outer RCM boundary is specified using the empirical model of Weimer (2001) that is driven by upstream solar wind and IMF data from NASA OMNIweb Plus. For the 17 March 2013 simulation run the Weimer potential at the outer boundary is scaled by the DMSP cross polar cap potential as explained in detail in (Chen et al., 2019), but for the 17 March 2015 event we did not have the DMSP cross polar cap potential readily available.

Following our earlier work (Chen et al., 2012) we assume that the electron and ion distributions at the outer boundary are kappa functions. For the 17 March 2015 simulation run we use the empirical plasma sheet model of Tsyganenko & Mukai (2003), based on statistical averages of ≤ 40-keV Geotail data, of density and temperature to specify the needed parameters of the kappa function at every 5 minutes. Protons with lower energies (e.g., ≤ 40 keV) typically contribute more to the density than ions with higher energies (e.g., ≥ 40 keV). However, from a previous study proton temperatures calculated from the THEMIS THA measurements over the energy range of 40 eV to 600 keV are about a factor of 2 larger than temperatures from measurements from 40 eV to 40 keV during 4-7 April 2010 (Chen, Lemon, Guild, et al., 2015; Keesee et al., 2014). For that reason, we scale the Tsyganenko & Mukai (2003) proton temperatures by a factor of 2. At the outer boundary it is assumed that the electron density equals the ion density. The boundary electron temperature is set as $T_e = T_p/7.2$, where T_p is the proton temperature, based on average central plasma sheet properties (Baumjohann et al., 1989). For the 17 March 2013 storm, we map LANL Magnetospheric Plasma Analyzer (MPA) (McComas et al., 1993) and Synchronous Orbit Particle Analyzer (SOPA) (Belian et al., 1992) electron and proton distributions at geosychronous orbit outward to 10 R_E to specify the parameters of their boundary kappa functions. The methodology is described in detail in (Chen et al., 2019). For this event, the O^+ density at the outer boundary is specified using the Kp-dependent relationship for the ratio of O^+ to proton density of Young et al. (1982). At the boundary the O^+ ion temperature is assumed to be equal to the proton temperature.

The Aerospace version of the RCM-E includes an initial electron distribution based on the empirical AE9 model (Ginet et al., 2013), the calculation of mean precipitating integrated electron energy flux from simulated phase space distributions (Chen, Lemon, Orlova, et al., 2015), and a simple plasmaspheric model in which the model plasmapause is determined from the simulated cold electron density n_e. We use the L-dependent plasmaspheric refilling rate for solar maximum of Denton et al. (2012).

2.1 Primary Precipitating Electron Flux

In Aerospace's version of the RCM-E the loss of electrons from interactions with magnetospheric waves are treated by using Kp and MLT-parameterized scattering rates based on statistical observations of wave properties with magnetic activity. Pitch-angle diffusion coefficients $D_{w\alpha\alpha}$ against whistler chorus were computed by Orlova & Shprits (2014) for electrons with energies E between 1 keV and 2 MeV for different Kp values over equatorial geocentric distances normalized by Earth radii R_0 from 3 to 8 and four magnetic local time (MLT) sectors from 21 MLT eastward to 15 MLT. They parameterized the quantity $1/D_{w\alpha\alpha}$ as functions of Kp, E, R_0, and MLT. Because the chorus wave diffusion coefficients are relatively monotonic, the scattering rate against the whistler chorus was set to be $\lambda_w = D_{w\alpha\alpha}$ outside the plasmasphere following (Shprits et al., 2006). A *Kp* and MLT-parameterization of the reciprocal of the pitch angle diffusion coefficients $D_{h\alpha\alpha}$ against plasmaspheric hiss waves was performed by Orlova et al. (2014) for electron energies between 1 keV and 10 MeV and for R_0 from 3 to 6. Inside the plasmasphere the scattering rate against plasmaspheric hiss is taken to be $\lambda_h = D_{h\alpha\alpha}$. A logarithmically weighted (by density) average of the lifetime against whistler chorus and hiss is used in the plasmapause region. In the spatial regions where there are no parameterizations of the scattering rate from (Orlova & Shprits, 2014) or (Orlova et al., 2014), we use a simple MLT-dependent lifetime given by (Chen and Schulz, 2001, hereafter referred to as CS). CS formulated an expression for the electron lifetime that smoothly transitions between weak diffusion in the plasmasphere and a fraction of strong diffusion in the plasma sheet. The strong diffusion lifetime τ_s is given by

$$\tau_s \approx [2\Psi B_h/(1-\eta)](\gamma m/p) \quad (1)$$

where Ψ is the flux-tube volume, B_h is the magnetic field intensity at the foot point of the field line, γ $(= m/m_0)$ is the ratio of the electron relativistic mass m to the rest mass m_0, and p is the particle momentum at an altitude h, η is taken to be a constant value of 2/3 so that electrons are lost at one third of the strong diffusion rate. The lifetime τ is given by

$$\tau = \begin{cases} [1+\lambda_w\tau_s]/\lambda_w \text{ for } n_e < 10\,\text{cm}^{-3}, \quad 0 \le \text{MLT} \le 15, \text{and } 21 \le \text{MLT} \le 24 \\ [1+\lambda_h\tau_s]/\lambda_h \text{ for } n_e > 100\,\text{cm}^{-3}, 3 \le R_0 \le 6 \text{ and all MLTs} \\ \dfrac{(\log(100)-\log(n_e))}{(\log(100)-\log(10))}\dfrac{[1+\lambda_w\tau_s]}{\lambda_w} + \dfrac{(\log(n_e)-\log(10))}{(\log(100)-\log(10))}\dfrac{[1+\lambda_h\tau_s]}{\lambda_h} \text{ for } 10\,\text{cm}^{-3} < n_e < 100\,\text{cm}^{-3}, \\ \quad 3 \le R_0 \le 6, 0 \le \text{MLT} \le 15, \text{and } 21 \le \text{MLT} \le 24 \end{cases} \quad (2)$$

Further details of the electron loss model used can be found in (Chen et al., 2015; 2019).

The RCM-E differential rate of energy deposition (per unit electron energy *E*) per unit area of the ionosphere is given by

$$(dQ/dE)_{prec} = \pi \left[\frac{2\Psi B_h\left(\frac{\gamma m}{p}\right)}{\tau}\right] |B_r/B_h| E p^2 f \qquad (3)$$

in units of $cm^{-2}s^{-1}$, where τ is given by (1), B_r is the radial component of the magnetic field at the foot of the flux tube and *f* is the phase space density. Within the square bracket of (3) is the ratio of the strong diffusion lifetime ((1) with η = 0) to the lifetime that is less than or equal to one. The RCM-E energy $E = \lambda\psi^{-2/3}$ (Harel et al., 1981), where λ is an invariant, depends on the flux tube volume, which is location dependent. For example, the electron energy can range from ~100 eV to ~1 or 2 MeV and includes the zero-energy electron channel for modeling cold plasma drift.

The integrated precipitating electron energy flux *Q* is obtained by integrating the energy times the differential energy flux over energy from a lower E_1 to upper E_2 limit as

$$Q = \int_{E_1}^{E_2} \left(\frac{dQ}{dE}\right)_{prec} dE. \qquad (4)$$

The mean energy of the precipitating electrons $\langle E \rangle$ is calculated from the precipitating differential particle flux $J(E) \equiv E^{-1} dQ/dE$ as

$$\langle E \rangle = \frac{\int_{E_1}^{E_2} J(E) E dE}{\int_{E_1}^{E_2} J(E) dE} = \frac{\int_{E_1}^{E_2} \left(\frac{dQ}{dE}\right) dE}{\int_{E_1}^{E_2} \left(\frac{dQ}{dE}\right)\left(\frac{1}{E}\right) dE}. \qquad (5)$$

For calculating the simulated ionospheric conductance we use energy limits of E_1 = 500 eV and E_2 = 30 keV in (5) and (6) that are consistent with the limits of integration of the Robinson et al. (1987) equations and the STET-modified Khazanov et al. (2019) equations. For calculating *Q* and $\langle E \rangle$ associated with observational data we use limits of integration appropriate to the instrument energy range.

2.2 M-I-A Coupled Precipitating Electron Flux

As the primary precipitating electrons deposit their energy into the ionosphere and thermosphere, complex coupled processes including the production of secondary electrons, back-scatter of primary and secondary electrons, and wave-particle scattering in the magnetosphere affect the dynamic precipitating electron flux spectra. The effect of these coupled magnetosphere-ionosphere-atmosphere processes are taken account of by modifying the primary precipitating electron distribution using relationships obtained through parameterized steady-state STET simulations.

The STET code comprehensively models various sources and collisional processes of electrons as they travel along an open or closed magnetic field line through the magnetosphere and ionosphere (Khazanov et al., 2015; Khazanov, Glocer, et al., 2016; Khazanov, Himwich, et al., 2016; Khazanov et al., 2017b). It can cover all latitudes and longitudes. The STET code applies two primary electron sources: photoelectrons generated through the interaction of solar extreme ultraviolet (EUV) and X-ray radiation with the neutral atmosphere, and precipitating electrons originating from the magnetosphere. It incorporates elastic and inelastic collisional processes between superthermal electrons and major neutral atmospheric components (N_2, O_2, and O) in the energy range of 1 eV to 50 keV.

Inputs to the STET code for the neutral thermospheric densities and temperatures were obtained from the MSIS-90 model (Hedin, 1991). The electron altitudinal profile in the ionosphere was derived based on the International Reference Ionosphere model (Bilitza et al., 2017) and extended into the plasmasphere region by assuming that the electron thermal density is proportional to the geomagnetic field ($n_e \sim B^2$). This approach represents an intermediate step during plasmaspheric refilling (Khazanov et al., 1984), particularly in large L-shells where electron diffuse aurora occurs. Cross sections for ionization, state-specific excitation, and elastic collisions were sourced from Solomon et al. (1988).

On closed field lines STET considers both magnetically conjugate regions when simulating the dynamic formation of electron distribution functions in a 1-D spatial and 2-D velocity space (energy and pitch angle). Previous STET simulations of diffuse precipitating electron flux distributions from primary Maxwellian electron spectra reach a steady state after 3 min (Khazanov and Glocer, 2020). Based on parametric steady state STET simulations of diffuse precipitating electron flux spectra in a dipole magnetic field with primary Maxwellian electron spectra, Khazanov et al. (2019) represented analytical functions that modify the primary Maxwellian integrated electron flux and mean energy that consider the MIA coupling and secondary electron effects. Following equations (3), (4), and (5) of Khazanov et al. (2019), the respective modified mean energy and modified integrated energy are

$$\langle E\rangle^{WMR} = 0.073 + 0.933 * \langle E\rangle - 0.0092 * \langle E\rangle^2 \qquad (6)$$

$$Q^{WMR} = K_c\,(\langle E\rangle)\,Q \qquad (7)$$

with

$$K_c = 3.36 - exp(0.597 - 0.37 * \langle E\rangle + 0.00794 * \langle E\rangle^2), \qquad (8)$$

where $\langle E\rangle$ is the mean energy of the primary Maxwellian spectrum with units of keV. We use the steady-state equations (6), (7), and (8) to modify the respective simulated RCM-E primary precipitating electron flux and mean energy at every 1 s. The storm-time RCM-E precipitating electron flux spectra are well represented by fits to Maxwellian distributions where the simulated diffuse aurora is robust, such as from pre-midnight to mid-morning (Chen et al., 2019). This is not necessarily true where the simulated diffuse aurora is weak, such as in the late afternoon or at very low latitudes. We impose a threshold integrated energy flux of 0.0316 erg/cm^2 for electrons and 0.0316 erg/cm^2 for ions for diffuse precipitation before computing the mean energy using (5) of the corresponding spectrum at each ionospheric grid point. The use of equations (6)-(8) are a reasonable estimate of the MIA coupling modifications to the RCM-E precipitating distributions.

2.3 Ionospheric Conductance Models

The modeled ionospheric conductance includes contributions from solar extreme ultraviolet (EUV) and ionization from precipitating diffuse auroral electrons and ions. We use the empirical IRI-2007 (Bilitza & Reinisch, 2008) model to specify the ionospheric conductance from EUV that is kept constant throughout a simulation run. Auroral conductance is calculated from simulated precipitating electron and ion fluxes that are updated every 1 s. From a previous simulation study, Chen et al. (2019) found that diffuse precipitating electrons are the dominant contributor to auroral conductance, whereas precipitating ions from FLC scattering tend to contribute significantly to the conductance locally and sporadically.

The Hall and Pedersen conductance for precipitating protons are computed using the empirical relations of Galand & Richmond (2001) that depend on the mean precipitated proton energy and integrated precipitating proton energy flux. For lack of any known available empirical relations between precipitating O^+ ions and ionospheric conductance, we estimate the conductance contribution from precipitating O^+ ions by applying the Galand & Richmond (2001) formulas. Details about the ion precipitation calculation can be found in Chen et al. (2019).

The auroral conductance contribution from simulated precipitating electrons are calculated by using either (A) interpolated results from the Boltzmann 3-Constituent (B3C) auroral transport code of Strickland et al. (1993) or (B) the simple empirical relations of Robinson et al. (1987) that depend on the mean precipitating electron energy and integrated electron energy flux. Method A is the primary approach while method B is used for comparison purposes with method A. As input for either method, we use RCM-E differential precipitating electron flux spectra to calculate the integrated and mean precipitating electron flux into the ionosphere without and with STET modifications (application of equations (6), (7), and (8)). The simulated RCM-E integrated electron energy flux and mean energy are then used to calculate the ionospheric conductance, using either method A or B, that is then fed back into the calculation of the electric potentials (see Figure 1).

With method A, Hall and Pedersen conductivity and height-integrated conductance are computed using the B3C auroral transport code of Strickland et al. (1993). The B3C code computes the coupled set of linear Boltzmann equations for electrons, protons, and H atom fluxes with full collisional processes (Basu et al., 1993) in a specified atmosphere over altitudes of 90 km to 500 km. An atmosphere based on the empirical NRLMSISE-00 model (Picone et al., 2002) with the geographic latitude, geographic longitude, daily Ap index, solar radio flux F10.7, and eighty-one-day F10.7 average (F10.7A) indices as inputs is used in the B3C for this study. The B3C code takes as input incident precipitating electron energy distributions at the upper boundary of 500 km for a specified geographic longitude and latitude. We assume an incident Maxwellian precipitating electron energy distribution with an associated energy flux *Q* and mean energy <*E*>. For a subset of the RCM-E grid points, the B3C is used to compute Hall and Pedersen conductivity altitude profiles and height-integrated conductance for daily Ap, F10.7, and F10.7A values corresponding to times of interest and for a wide range of <*E*> and *Q* parameters. The values are saved in a look-up table for selected times during two magnetic storms: (1) every 3 hours between 17 March 2013

00:00 UT and 18 March 2013 06:00 UT and (2) approximately every 3 hours between 17 March 2015 00:00 UT and 19 March 2015 00:00 UT, with slight deviations from a 3-hour cadence when the time scale of changes to the B3C inputs warrants shorter intervals (during the main phase) or allows for longer ones (during the recovery phase, especially the late recovery phase). For any given RCM-E grid point and time, the RCM-E interpolates the values of the Hall and Pedersen conductance from the tables and these values are used to compute the RCM-E ionospheric potential that is self-consistent with the particle transport. This is done for simulated precipitating mean electron energies and integrated energy fluxes with (Q^{WMR} and $<E>^{WMR}$) and without (Q and $<E>$) the STET modifications. The interpolation of the B3C conductivity conductance tables is a computationally feasible approach to calculating altitudinal profiles of conductivity.

Method B is to calculate the ionospheric auroral electron conductance from the simple empirical formulas of Robinson et al. (1987):

$$\Sigma_{\boldsymbol{P}} = \frac{40\langle E\rangle}{16+\langle E\rangle^2}\, Q^{1/2} \tag{9}$$

$$\frac{\Sigma_{\boldsymbol{H}}}{\Sigma_{\boldsymbol{P}}} = 0.45\,\langle E\rangle^{0.85}, \tag{10}$$

where we use the simulated integrated electron energy flux Q and mean energy $\langle E\rangle$ with or without the STET modification for MIA coupling effects.

3 Observational Data

3.1 Poker Flat Research Range

The Poker Flat Research Range (PFRR) in Alaska is located at (65.1° N geographic latitude, 212.5° E geographic longitude, 65.9° magnetic latitude). The Poker Flat Incoherent Scatter Radar (PFISR) is a phased-array incoherent scatter radar radar capable of beamsteering on a pulse-to-pulse basis, which is also located at PFRR (Valentic et al., 2013). PFISR produces estimates of the altitude-resolved electron density and line of sight (LOS) velocities from which the electric field can be estimated using the methodology described in (Heinselman & Nicolls, 2008). The Pedersen and Hall conductance, i.e., altitude integrated conductivity, are estimated using electron density observations from the field-aligned beam at PFISR. Approximate forms were used that are valid above 100 km altitude for the Hall and Pedersen conductivities; more details on the conductivity calculations can be found in (Kaeppler et al., 2023). The electric field was derived using the F-region line-of-sight velocities. We produced a single estimate of the electric field from the F-region LOS velocities, instead of the more typical 1-D vector electric field (electric field vs. magnetic latitude). This single F-region electric field is suitable for large-scale model data comparisons since the 1-D electric fields correspond to a single model grid point. Using a single vector electric field was used in (Meng et al., 2022) and we use a similar method in this investigation.

The Aerospace Corporation has operated a 4-channel photometer system at PFRR. The details of the system including calibration data analysis techniques have been described in (Hecht et al., 2008; Hecht et al., 2012). For the purposes of this study the two key parameters are the integrated energy flux Q_{PF} and mean energy $\langle E_{PF} \rangle$ of the precipitating electrons over energies of 100 eV to 14 keV.

The photometer data are essentially measuring the auroral emission at night over a narrow field of view (<2°) pointed up the nominal magnetic field line direction at PFRR. During periods of diffuse aurora, typically associated with Maxwellian energy distributions, the instrument often detects somewhat constant or slow temporal variations in Q_{PF} and $\langle E_{PF} \rangle$ that are not correlated. However, during periods of discrete aurora, typically associated with Gaussian energy distributions, observations usually reveal rapid and large variations in Q_{PF} and often in $\langle E_{PF} \rangle$ as

Q_{PF} and $\langle E_{PF} \rangle$ are correlated. This is discussed further in (Christensen et al, 1987; Hecht et al., 1999; Hecht et al, 2008).

3.2 Millstone Hill Geospace Facility

The Massachusetts Institute of Technology (MIT) Millstone Hill Geospace Facility (MHGF) is at Westford, Massachusetts at (42.6° geodetic latitude; 288.5° geodetic longitude; 54° magnetic latitude). The Millstone Hill incoherent scatter radar observations during the 2013 and 2015 St. Patrick's Day storms were previously described by Foster et al. (2014) and Zhang et al. (2017). Utilizing the plasma density and temperature data from the radar's zenith antenna, along with empirical models NRLMSISE-00 [Picone et al., 2002] and IRI [Bilitza and Reinisch, 2008], Zhang et al. (2017) estimated the integrated Pedersen and Hall conductivities over Millstone Hill in both the E region (100–150 km) and F region (200–550 km), as well as the total conductivity over the 100–550 km range during the 2015 event. The same methodology was employed in the present study as well as in the Madrigal database (Rideout W., Cariglia K. CEDAR Madrigal Database URL: http://cedar.openmadrigal.org).

4 Simulation Results and Data-Model Comparisons

We simulate the 17 March 2013 (min *Dst* = –131 nT) and 17 March 2015 (min *Dst* = –233 nT) storms using RCM-E, STET-modifications, and B3C, hereafter referred to as RCM-E, STET, B3-C for shorthand, to examine the effects of diffuse auroral precipitation on spatial and temporal variations of conductivity and conductance during these magnetic storms. These two storms began in equinox on the same day of different years and thus had similar solar illumination and ionospheric conditions. However, the 17 March 2015 storm was more intense than the 17 March 2013 storm because of enhanced solar wind driving. According to several citizen observations reported by Case & MacDonald (2015), the aurora associated with the Saint Patrick's Day 2015 storm was visible at low latitudes. For both events the simulated Hall and Pedersen conductance are compared with conductance inferred from ISR data from Poker Flat. Model conductance and conductance inferred from ISR data from Millstone Hill, which is at a lower magnetic latitude than Poker Flat, are also compared for the larger 17 March 2015 storm.

4.1 Saint Patrick's Day 2013 Storm

The St. Patrick's Day 2013 storm was driven by a large coronal mass ejection (CME) observed on 17 March 2013 at 06:28 UT by NASA's Advanced Composition Explorer (ACE). Figure 2 shows the geomagnetic SYM-H index (a one-minute resolved *Dst* measurement), solar wind dynamic pressure, and interplanetary magnetic field (IMF) during 17–18 March 2013. The data shown in Figures (a)–(e) were downloaded from the NASA OMNIWeb: https://omniweb.gsfc.nasa.gov/ow_min.html. On 17 March 2013 the solar wind dynamic pressure (Figure 2b) became elevated around 5:20 UT leading to the storm's sudden commencement when SYM-H (Figure 2e) reached 26.5 nT. The storm main phase started around 6:30 UT and lasted for approximately 14 hr with a minimum SYM-H of –132 nT attained at 21:00 UT. This was followed by a recovery phase when the IMF B_z (Figure 2e) was positive.

The storm simulation includes time-dependent boundary conditions described in Section 2. Variations of the RCM-E electric boundary conditions specified at 10 R_E and 00:00 MLT in the plasma sheet are shown in Figure 2f. The electric potential at the midnight boundary is enhanced during the storm main phase and reaches a maximum value of 264 kV. The time-dependent electron, proton, and O^+ ion densities (not including the plasmasphere component) at the midnight boundary are shown in Figures 2g. The electron density at the boundary was generally elevated during the storm main phase.

Features of the simulated diffuse precipitating electron energy flux in the ionosphere at 850 km during the storm are illustrated in Figures 3a, 3b, and 3c. The ordinate of the plots is MLAT from 45° to the quiet time high latitude boundary of 67.5° and the abscissa is MLT. The dashed gray curves correspond to *L* values from 3 to 7 and the white curve represents the model plasmapause. Representative pre-storm (17 March, 06:00 UT), early main phase (17 March, 08:00 UT) and late main phase (17 March, 20:00 UT) results are shown. Note that the high latitude boundary of the RCM-E simulation has moved to lower latitudes on the nightside because the field lines stretch during the storm (the 10 R_E boundary maps to lower latitudes). The precipitating electron energy flux tends to be relatively intense from ~21:00 MLT through midnight to the morning and less concentrated from the afternoon to around dusk. This is because most of the plasma sheet electrons are scattered by whistler chorus waves and precipitate before they can gradient-curvature drift to the afternoon side (Chen and Schulz, 2001; Chen et al., 2019). The precipitation occurs predominantly outside the plasmasphere (poleward of the white curve) where the lifetimes against scattering with whistler waves (Orlova & Shprits, 2014) are generally shorter than the lifetimes against plasmaspheric hiss (Orlova et al., 2014) for a given energy, *L* and Kp value. Early in the storm main phase at 08:00 UT, the spatial region of the precipitating electron flux on the night side had extended to lower latitudes and the maximum precipitating electron flux was more intense as compared to pre-storm at 06:00 UT. By late storm main phase at 20:00 UT the spatial extent of electron energy flux had broadened in MLAT and MLT compared to at 08:00 UT. The model plasmapause shows features of a plume, as labeled in Figure 3c. Equatorward of the plasmapause from ~17:00 MLT to ~22:00 MLT there is energy flux associated with electrons that had precipitated to that region earlier.

The simulated Hall and Pedersen conductance for the three representative times are shown in Figures 3d-3f and 3g-3i, respectively. The Hall and Pedersen conductance associated with EUV on the dayside is kept constant throughout the simulation. For each time of interest shown, the simulated auroral Hall and Pedersen conductance are similar in spatial extent as the corresponding precipitating electron energy flux (e.g., compare Figures 3d and 3a). However, the magnitude of the most intense auroral Pedersen conductance is smaller than the corresponding most intense auroral Hall conductance.

Ionospheric conductance and field-aligned currents affect the electric field. The simulated electric intensity $|\mathcal{E}|$ at 850 km at different times are shown in Figures 3j-3l where the gray curves are constant equipotential contours spaced by 2 kV/contour. The equipotential contours in the pre-storm electric intensity at 06:00 UT (Figure 3j) show a two-cell convection pattern at auroral latitudes. The region of enhanced convection extends to lower latitudes by the late main phase (Figure 3l). The electric intensity is large from about dusk to midnight in the region of low conductance that is equatorward of the high to low conductance boundary. This is a feature of the electric field associated with westward subauroral polarization streams (SAPS) (Foster and Burke, 2002). There are large electric intensities near dawn associated with eastward dawnside subauroral polarization streams (DAPS). Lin et al. (2022) have shown through simulations and DMSP observations of a large storm event that DAPS can occur during intense storms when the magnetospheric convection is large enough to transport ions directly from the plasma sheet toward low L-shells near dawn; rather than being diverted to the dusk side by energy-dependent gradient drifts.

Figures 4a–4d show examples of simulated altitudinal profiles of the auroral Pedersen and Hall conductivity σ versus magnetic local time at 60° MLAT for the 17 March 2013 storm. During the early storm main phase at 08:00 UT, the Pedersen (Figure 4a) and Hall (Figure 4c) conductivity exceed 1.0 x 10^{-4} S/m from pre-midnight (≈ 22:30 MLT) to early morning (≈ 4:30 MLT) at altitudes of about 110 km to 150 km and 100 km to 140 km, respectively. Late in the main phase at 20:00 UT, the Pedersen (Figure 4b) and Hall (Figure 4d) conductivity exceed 1.0 x 10^{-4} S/m over a broader range of MLTs than at 08:00 UT. At a fixed magnetic latitude in the auroral zone, the time evolution of the magnetic local distribution of the conductivity enhancement is consistent with the MLT distribution of the precipitating electron energy flux (cf. Figures 3b and 3c).

As electrons precipitate, they deposit energy to the high-latitude atmosphere that leads to heating. This simulated particle heating per unit volume rate is calculated from the derivative of the electron energy flux with respect to altitude *z*,

$$W_{\mathrm{p}} = \mathrm{d}Q/\mathrm{d}z. \qquad (11)$$

The simulated particle heating profile at 60° MLAT is significantly enhanced from 100 km to roughly 180 km at 08:00 UT (Figure 4e) and at 20:00 UT (Figure 4f). At a fixed auroral MLAT, the MLT distribution of the simulated particle heating rate is like that of the precipitating electron energy flux. Neglecting effects of neutral winds, the joule heating rate is

$$W_{\mathrm{J}} = \sigma_{\mathrm{ped}}|\mathcal{E}|^2. \qquad (12)$$

At 08:00 UT (Fig. 4g), the most intense joule heating occurs around 100 km to 200 km and from ≈ 21:00 MLT to 5:00 MLT. By 20:00 UT (Fig. 4h), enhanced joule heating occurs from ≈15:00 MLT to 10:30 MLT. The simulated joule heating dominates particle heating where the Pedersen conductivities were relatively low and the electric intensity in the regions indicated by the arrows in Figure 4g and 4h.

We compare the simulated ionospheric conductance and electric intensity with observations from the PFRR. The black diamonds in Figure 5a and 5b show the respective Poker Flat ISR

(PFISR) Pedersen and Hall conductance during the storm. Figure 5f shows the time trace of SYM-H (black curve) and the MLT (dashed green curve) for reference. From 00:00 UT to 06:00 UT (≈12:00 MLT to 08:00 MLT) on 17 March, the pre-storm PFISR Pedersen conductance is below 10 S and the PFISR Hall conductance is below 12 S. During the storm main phase, the PFISR Pedersen and Hall conductance are significantly enhanced to values as high as 38 S and 90 S, respectively. As the storm recovers the PFISR Pedersen and Hall conductance gradually trended downward toward pre-storm levels.

The RCM-E-STET-B3C simulated Pedersen and Hall conductance (pink curve) at the PFRR magnetic latitude of 65.9° are plotted over the corresponding PFISR conductance in Figures 5a and 5b. Also shown are results from simulations using RCM-E with STET and the Robinson et al. formulas for calculating conductance (orange curve), RCM-E without STET and the Robinson et al. formulas (blue curve), and RCM-E without STET and B3C (cyan curve). There is a gap in the model results because the RCM model boundary at 10 R_E maps to latitudes below 65.9° as the field lines are stretched on the nightside during the main phase. The RCM-E-STET-B3C Pedersen and Hall conductance agree reasonably well with the respective PFISR conductance before the storm (00:00 UT to 06:00 UT) when the conductance is primarily due to EUV and between 18:00 UT (~07:00 MLT) to 23:00 UT (~12:00 MLT) on 17 March 2013 where we expect stormtime diffuse aurora to be present. During 18:00 UT to 23:00 UT, the PFISR conductance shows some impulsive enhancements above the simulated conductance values that we interpret as being associated with discrete aurora.

During pre-storm, PFRR is on the dayside at ≈12:00 MLT to 18:00 MLT when the effects on conductance from EUV likely dominate over auroral precipitation. The RCM-E-STET-B3C and RCM-E-B3C Pedersen/Hall conductance are virtually identical and higher than the RCM-E-STET-Robinson and RCM-E-Robinson Pedersen/Hall conductance that are similar (Figure 5a and 5b) during pre-storm. The conductance on the dayside calculated from the B3C code is higher than the empirical IRI-2007 model.

The photometer observations of rapid and large fluctuations in the Q_{PF} and $<E_{PF}>$ during the storm main phase (Figures 5c and 5d) seem to be consistent with discrete rather than diffuse aurora. The most likely period of diffuse aurora is after 1330 UT on 17 March. PFRR does keep an archive of their all sky auroral movies online (http://optics.gi.alaska.edu/realtime/data/MPEG/PKR_DASC_256/) and the movie for 17 March 2013 is mostly consistent with this interpretation. The big fluctuations in Q_{PF} and $<E_{PF}>$ occur when there are the enhancements in PFISR Pedersen and Hall conductance. The simulated Q and $<E>$ (equations (4) and (5)) are also plotted in Figures 5c and 5d, but because of the gap in the model results they were not available when the photometer measurements were.

During the late storm main phase to early recovery phase (≈17:00 UT on 17 March to 00:00 UT on 18 March), simulated Q that included the STET atmospheric backscatter effects were generally larger than simulated energy flux that did not include STET modifications (Figure 4c). The inclusion of atmospheric backscatter has an energy cascading effect that tends to decrease the mean energy of the precipitating spectrum (e.g., Figure 1 of Khazanov et al., 2019). Thus, the RCM-E-STET-B3C $<E>$ is lower than the RCM-E-B3C $<E>$ and the RCM-E-STET-Robinson $<E>$ is lower than the RCM-E-Robinson $<E>$ in Figure 5d. As noted earlier, the respective STET-modified Q and $<E>$ are calculated over the energy range of 500 eV to 30 keV following Robinson et al. (1987). The <500-eV and > 30-keV tails of the modified precipitating electron distribution do not significantly contribute to the ionospheric conductance.

The rapidly fluctuating PF electric intensity Ɛ (Figure 5e) is below 25 mV/m during pre-storm and on the dayside but is significantly enhanced during the storm main phase, then decreases overall during the recovery phase. The RCM-E-STET-B3C and RCM-E-B3C electric intensity show similar trends with good agreement during pre-storm and recovery phases and reasonable order of magnitude agreement during the late main phase. There are big spikes in the model Ɛ during the sudden commencement and very early main phase (6:00 UT to 7:00 UT; ≈18:00 MLT) that overestimate the observed Ɛ. Significant enhancements in simulated Ɛ are associated with low modeled conductance near dusk during the early main phase of the March 17, 2013 storm, as discussed previously by Khazanov et al. (2019). Our model does not account for conductance associated with discrete aurora driven by field-aligned potential drops. However, the presence of such discrete auroral conductance could supplement the low conductance from diffuse aurora, potentially reducing the simulated Ɛ.

4.2 Saint Patrick’s Day 2015 Storm

The Saint Patrick's Day storm of 2015 was triggered by a coronal mass ejection (CME) that occurred on 17 March 2015, at 02:00 UT. Figure 6 shows variations of SYM-H, solar wind and IMF data for this event that were obtained from NASA OMNIWeb: omniweb.gsfc.nasa/gov/ow_min.html. The storm’s main phase started at 06:55 UT and unfolded in two distinct steps (Figure 6a). The first step involved a decrease in SYM-H of 100 nT, driven by the southward IMF (Figure 6e) in the sheath region (Kataoka et al., 2015). The second step, driven by the southward IMF in the magnetic cloud, saw SYM-H drop to a minimum value of –233 nT, with the maximum solar wind dynamic pressure reaching 21.2 nPa (Figure 6b). This was followed by a recovery phase lasting approximately two days.

Intervals of significant enhancement of the RCM-E electric potential from pre-storm values at the 10 R_{E} boundary in the plasma sheet (Figure 6f) during the main phase are consistent with the periods when the IMF was southward. The respective electron, proton, and O^+ ion density (not including the plasmasphere component) at the midnight model boundary at 10 $\mathrm{R_E}$ are shown in Figure 6g.

MLAT versus MLT maps of the RCME-STET-B3C simulated electron energy flux at 850 km in the ionosphere during the early storm main phase (09:00 UT on 17 March 2015; Figure 7a), late main phase (19:00 UT on 17 March 2015; Figure 7b), and recovery phase (18:00 UT on 18 March 2015; Figure 7c) show simulated diffuse precipitation with energy flux > 10 $\mathrm{erg/cm^2}$ at latitudes as low as 44° MLAT at 04:00 MLT during the late main phase of this large storm. Enhancements in the simulated Hall and Pedersen conductance occur at latitudes as low as 46° MLAT at 04:00 MLT at 19:00 UT on 17 March 2015 (Figures 7e and 7h). Figure 7i illustrates large simulated electric intensities associated with westward SAPS from ≈ 14:00 MLT toward midnight and with eastward DAPS near dawn. The indentations in the model plasmapause (white curve) in Figures 7c, 7f, and 7i during the recovery phase at 18:00 UT on 18 March 2015 correspond to the boundary of a plasmaspheric plume with no significant electron precipitation within the plume.

Variations in the simulated Pedersen and Hall auroral conductance, electron pressure, ion pressure, FAC, and electric intensity at subauroral to auroral latitudes for representative fixed magnetic local times on the nightside during the Saint Patrick's Day 2015 storm are displayed in Figure 8. The Pedersen (Figures 8a–8d) and Hall (Figures 8e–8h) conductance are elevated at auroral latitudes during the storm main phase and are significantly diminished by the late recovery phase. At 21:00 MLT and at 00:00 MLT, there are latitudinal gaps in the simulated Pedersen (Figures 8a and 8g) and Hall auroral conductance (Figures 8b and 8h) associated with a plasmaspheric plume formed during the recovery phase. In contrast to the auroral conductance, the simulated electron (Figures 8i–8l) and ion (Figures 8m–8p) pressure associated with the trapped population is concentrated at lower latitudes. During the main phase, the electron pressure at 21:00 MLT (Figure 8j) is relatively low as many electrons from the nightside plasma sheet drift eastward from the energy- and charge-dependent drift to lower *L* values. The main phase electron pressure tends to strengthen towards increasing lower latitudes at midnight to dawn (00:00 MLT, 03:00 MLT, and 06:00 MLT; Figures 8k–8m). In contrast, the main phase simulated ion pressure at pre-midnight to midnight (21:00 MLT or 00:00 MLT) are more intense than at early morning or dawn (03:00 MLT or 06:00 MLT) as many ions from the nightside plasma sheet drift westward to lower *L* values. Figures 8q – 8t illustrate the time evolution of the simulated FACs where blue/red corresponds to field-aligned currents going into/out of the ionosphere. During the main phase at 21:00 MLT, the electric intensity associated with SAPS gets relatively large equatorward (Figure 8u) of the low-high conductance boundary where the ion pressure significantly exceeds the electron pressure and strong FACs are going into the ionosphere. At 00:00 MLT and 03:00 MLT the main phase electric intensity is strong where the FACs are flowing into the ionosphere and where the ion pressure significantly exceeds the electron pressure.

Examples of the spatial variation of the simulated Pedersen conductivity, Hall conductivity, and particle and joule heating during the early and late main phase of the 17 March 2015 storm are shown in Figure 9. Focusing on altitudes of about 110 km to 150 km, relatively large Pedersen and Hall conductivities and particle heating occur from ≈22:00 MLT to 06:00 MLT at 60° MLAT at 08:00 UT. In contrast, the Pedersen and Hall conductivity and particle heating at a lower MLAT of 52.8° is relatively very small early in the main phase at 08:00 UT.

By 22:00 UT in the late main phase, there are relative enhancements in the conductivities and particle heating at 110 km to 150 km and 60° MLAT at all local times. Over the same altitudinal range at 52.8° MLAT, relative increases in the conductivities and particle heating occur from about 22:00 MLT to 06:00 MLT. The simulated joule heating is relatively stronger at 60° MLAT than at 52.8° MLAT for the representative times of 08:00 UT and 22:00 UT during the main phase. This is consistent with |E| being stronger at 60° MLAT than at 52.8° MLAT (see Figures 8u – 8x) and the joule heating being proportional to the |Ɛ|^{2}.

We compare the RCME-STET-B3C ionospheric conductance and Ɛ with observations from the PFRR at 65.9° MLAT for the St. Patrick's Day 2015 storm in Figure 10. From 00:00 UT to 05:00 UT on 17 March 2015 during pre-storm, the PFISR Pedersen and Hall conductance (black diamonds in Figures 10a and 10b) is less than 8 S and 9 S, respectively. From ≈ 5:00 UT to 13:00 UT the PFRR ISR and photometer data are not good because of the presence of clouds. The respective Pedersen/Hall conductance spiked as high as about 38 S/75 S during the storm main phase and about 30 S/72 S during the recovery phase. The large fluctuating enhancements in the conductance are associated with discrete aurora observed in the PFRR all-sky camera movie not shown here. There are extended periods of time with moderate conductance values when there was diffuse aurora from dusk to dawn. The simulated Pedersen/Hall conductance (pink curves) agree reasonably well with the PFISR Pedersen/Hall conductance during these periods associated with diffuse aurora. However, the simulated Pedersen/Hall conductance underestimates spikes in the PFISR Pedersen/Hall conductance such as at 19:30 UT on 17 March 2015. The simulated Pedersen/Hall conductance also agrees well with the pre-storm PFISR Pedersen/Hall conductance. The PFISR | Ɛ |, displayed as the black curve in Figure 10e, has high-frequency fluctuations. The simulated |E| follows some of the general trends of the PFISR |E| surprisingly well given that the simulated electric field is updated every 5 minutes.

From citizen science photos of diffuse auroral glows over Williamstown, MA and over Cape Cod, MA during the St. Patrick's Day 2015 event (around 1:00 to 3:00 UT on March 18, 2015) (Freedman, 2015), it is very likely that there was diffuse aurora over MHGF at 52.5° MLAT at the same time. The black diamonds in Figures 11a and 11b show the Millstone Hill (MH) ISR Pedersen and Hall conductance, respectively. The green line in Figure 11c is the MLT of MHGF. From 15:00 UT to 21:00 UT on March 17, MHGF is on the dayside where the Pedersen and Hall conductance is from EUV. On the dayside, the model conductance based on IRI-2007 specifications underestimates the MHGF conductance. Between dusk (21:00 UT on March 17; late main phase) to 23:00 MLT (4:00 UT on March 18; early recovery phase), the weak diffuse auroral precipitation contributes to simulated Pedersen and Hall conductance at low latitudes 52.5° MLAT where the simulated conductance agrees reasonably, well with the corresponding MHGF conductance. Unfortunately, MHISR measurements were unavailable on the early morning side near dawn during the storm main phase where diffuse aurora is expected to be more intense. Nonetheless, the RCME-STET-B3C Pedersen/Hall conductance agree with the MHISR Pedersen/Hall conductance within a factor of 2 for the example shown in Figure 11.

5 Summary and Conclusions

We investigated the impact of storm-time diffuse auroral electron precipitation on ionospheric Pedersen and Hall conductivities and conductance during the CME-driven St. Patrick's Day storms of 2013 (min Dst = –131 nT) and 2015 (min Dst = –233 nT). Simulations were conducted using the magnetically and electrically self-consistent RCM-E model, with STET modifications to account for backscatter, and the B3C auroral transport code to calculate conductivities and height-integrated conductance. These simulated results were validated against conductance inferred from PFISR and MHISR measurements and Themis ASI data. The main findings are summarized as follows:

1. The MLAT (magnetic latitude) and MLT (magnetic local time) distributions of simulated ionospheric Pedersen and Hall auroral conductance and diffuse precipitating electron energy flux show a strong similarity at given times during the storm events. The model plasmapause, which can include plasmaspheric plumes, represents the low-latitude boundary of auroral conductance.
2. The simulated Pedersen and Hall conductance agrees reasonably well with corresponding Pedersen and Hall conductance derived from PFISR measurements at 65.9° MLAT for both storm events when diffuse aurora is present. A comparison with Hall conductance derived from Themis ASI is needed to complete the analysis.
3. During the intense St. Patrick's Day 2015 storm, an extended period of diffuse aurora reached the MHGF at 52.5° MLAT. Simulated Pedersen and Hall conductance agreed within a factor of two with the MHISR Pedersen and Hall conductance.
4. PFRR all-sky camera footage shows the presence of discrete auroral arcs during both storm events (http://optics.gi.alaska.edu/realtime/data/MPEG/PKR_DASC_256/). The PFISR-derived conductance significantly increased, reaching up to several tens of siemens during discrete aurora episodes. These enhancements due to discrete auroral precipitation are not captured by the simulation model, which focuses only on diffuse aurora. At a fixed auroral MLAT, the largest storm-time enhancements occur in the simulated Pedersen conductivity between approximately 110 km and 160 km altitude and in Hall conductivity between about 100 km and 140 km altitude.

5. The simulations revealed the development of storm-associated electric field enhancements, specifically those linked to sub-auroral polarization streams and dawn sub-auroral polarization streams, during both storm events.
6. The simulated electric field intensity closely follows the general trend of the PFRR-derived electric field intensity at 65.9° MLAT when diffuse aurora is present during both storms, despite the simulations updating the electric field every five minutes.

Overall, the reasonable agreement between the simulated ionospheric conductance and conductance inferred from PFISR and MHISR measurements during periods of diffuse auroral precipitation is encouraging. However, future advancements in ionospheric conductivity, conductance, and electric field modeling will require a deeper understanding of the effects of discrete auroral precipitation, which is currently not accounted for in these simulations.

Data Statement

Data used in publishing this study are available at https://doi.org/10.5281/zenodo.15178684 (Chen et al., 2025).

Acknowledgments and Data

Five-minute upstream solar wind and IMF data used in this study are obtained from the NASA OMNIWeb Plus at https://omniweb.gsfc.nasa.gov/index.html. M. W. Chen was supported by the NSF grant AGS 225404, NASA awards 80NSSC21K1552, NNH19ZDA001NHGIO and 80NSSC24K1103. Millstone Hill ISR observation and the Madrigal database system are provided to the community by MIT under the support of NSF award AGS-1952737. S.-R. Zhang was also supported by NASA grants 80GSFC22CA011, 80NSSC21K1310, and 80NSSC22K1013, as well as NSF award AGS-2033787.

References

Basu, B., Jasperse, J. R., Strickland, D. J., & Daniell, R. E. (1993). Transport-Theoretic Model for the Electron-Proton-Hydrogen Atom Aurora, 1. Theory. Journal of Geophysical Research, 98(A12), 21517–21532. https://doi.org/10.1029/93JA01646

Baumjohann, W., Paschmann, G., & Cattell, C. A. (1989). Average plasma properties in the central plasma sheet. Journal of Geophysical Research: Space Physics, 94(A6), 6597–6606. https://doi.org/10.1029/JA094iA06p06597

Belian, R. D., Gisler, G. R., Cayton, T., & Christensen, R. (1992). High-Z energetic particles at geosynchronous orbit during the Great Solar Proton Event Series of October 1989. Journal of Geophysical Research: Space Physics, 97(A11), 16897–16906. https://doi.org/10.1029/92JA01139

Bilitza, D., Altadill, D., Truhlik, V., Shubin, V., Galkin, I., Reinisch, B., & Huang, X. (2017). International Reference Ionosphere 2016: From ionospheric climate to real-time weather predictions: IRI-2016. Space Weather, 15(2), 418–429. https://doi.org/10.1002/2016SW001593

Bilitza, D., & Reinisch, B. W. (2008). International Reference Ionosphere 2007: Improvements and new parameters. Advances in Space Research, 42(4), 599–609. https://doi.org/10.1016/j.asr.2007.07.048

Brekke, A., Doupnik, J. R., & Banks, P. M. (1974). Incoherent scatter measurements of E region conductivities and currents in the auroral zone. Journal of Geophysical Research (1896-1977), 79(25), 3773–3790. https://doi.org/10.1029/JA079i025p03773

Case, N. A., & MacDonald, E. A. (2015). Aurorasaurus and the St Patrick's Day storm. Astronomy & Geophysics, 56(3), 3.13-3.14. https://doi.org/10.1093/astrogeo/atv089

Chen, M. W., Lemon, C. L., Guild, T. B., Keesee, A. M., Lui, A., Goldstein, J., Rodriguez, J. V., & Anderson, P. C. (2015). Effects of modeled ionospheric conductance and electron loss on self-consistent ring current simulations during the 5-7 April 2010 storm: ELECTRON LOSS EFFECTS ON RING CURRENT. Journal of Geophysical Research: Space Physics, 120(7), 5355–5376. https://doi.org/10.1002/2015JA021285

Chen, M. W., Lemon, C. L., Guild, T. B., Schulz, M., Roeder, J. L., & Le, G. (2012). Comparison of self-consistent simulations with observed magnetic field and ion plasma parameters in the ring current during the 10 August 2000 magnetic storm: DATA-MODEL COMPARISONS OF RING CURRENT. Journal of Geophysical Research: Space Physics, 117(A9), n/a-n/a. https://doi.org/10.1029/2012JA017788

Chen, M. W., Lemon, C. L., Hecht, J., Sazykin, S., Wolf, R. A., Boyd, A., & Valek, P. (2019). Diffuse Auroral Electron and Ion Precipitation Effects on RCM-E Comparisons With Satellite Data During the 17 March 2013 Storm. Journal of Geophysical Research: Space Physics, 124(6), 4194–4216. https://doi.org/10.1029/2019JA026545

Chen, M., Lemon, C., Hecht, J., Khazanov, G., Evans, J. S., Kaeppler, S., Gabrielse, C., & Zhang, S.-R. (2025). Data for manuscript "Diffuse Auroral Precipitation Effects on Ionospheric Conductance During Magnetic Storms: Comparison of Simulated and Incoherent Radar Scatter-Inferred Conductance" [Data set]. Zenodo. https://doi.org/10.5281/zenodo.15178684

Chen, M. W., Lemon, C. L., Orlova, K., Shprits, Y., Hecht, J., & Walterscheid, R. L. (2015). Comparison of simulated and observed trapped and precipitating electron fluxes during a magnetic storm: SIMULATED AND OBSERVED ELECTRON FLUXES. Geophysical Research Letters, 42(20), 8302–8311. https://doi.org/10.1002/2015GL065737

Chen, M. W., & Schulz, M. (2001). Simulations of diffuse aurora with plasma sheet electrons in pitch angle diffusion less than everywhere strong. Journal of Geophysical Research: Space Physics, 106(A12), 28949–28966. https://doi.org/10.1029/2001JA000138

Christensen, A. B., Lyons, L. R., Hecht, J. H., Sivjee, G. G., Meier, R. R., & Strickland, D. G. (1987). Magnetic field-aligned electric field acceleration and the characteristics of the optical aurora. Journal of Geophysical Research: Space Physics, 92(A6), 6163–6167. https://doi.org/10.1029/JA092iA06p06163

Ebihara, Y. (2004). Postmidnight storm-time enhancement of tens-of-keV proton flux. Journal of Geophysical Research, 109(A12). https://doi.org/10.1029/2004JA010523

Ebihara, Y., & Fok, M.-C. (2004). Postmidnight storm-time enhancement of tens-of-keV proton flux. Journal of Geophysical Research: Space Physics, 109(A12). https://doi.org/10.1029/2004JA010523

Freedman, A. (2015, March 18). Photos: Spectacular aurora from severe solar storm light up northern skies. The Washington Post. Retrieved from https://www.washingtonpost.com/news/capital-weather-gang/wp/2015/03/18/photos-spectacular-aurora-from-severe-solar-storm-light-up-northern-skies/

Foster, J. C., and W. J. Burke (2002), SAPS: A new categorization for sub-auroral electric fields, *Eos Trans*. AGU, 83(36), 393–394, doi:10.1029/2002EO000289.

Foster, J. C., P. J. Erickson, A. J. Coster, S. Thaller, J. Tao, J. R. Wygant, and J. W. Bonnell (2014), Storm time observations of plasmasphere erosion flux in the magnetosphere and ionosphere, *Geophys. Res. Lett.*, 41, 762–768, doi:10.1002/2013GL059124.

Fuller-Rowell, T. J., & Evans, D. S. (1987). Height-integrated Pedersen and Hall conductivity patterns inferred from the TIROS-NOAA satellite data. Journal of Geophysical Research: Space Physics, 92(A7), 7606–7618. https://doi.org/10.1029/JA092iA07p07606

Galand, M., & Richmond, A. D. (2001). Ionospheric electrical conductances produced by auroral proton precipitation. Journal of Geophysical Research: Space Physics, 106(A1), 117–125. https://doi.org/10.1029/1999JA002001

Ginet, G. P., O'Brien, T. P., Huston, S. L., Johnston, W. R., Guild, T. B., Friedel, R., Lindstrom, C. D., Roth, C. J., Whelan, P., Quinn, R. A., Madden, D., Morley, S., & Su, Y.-J. (2013). AE9, AP9 and SPM: New Models for Specifying the Trapped Energetic Particle and Space Plasma Environment. The Van Allen Probes Mission, 579–615. https://doi.org/10.1007/978-1-4899-7433-4_18

Hardy, D. A., Gussenhoven, M. S., & Brautigam, D. (1989). A statistical model of auroral ion precipitation. Journal of Geophysical Research: Space Physics, 94(A1), 370–392. https://doi.org/10.1029/JA094iA01p00370

Hardy, D. A., Gussenhoven, M. S., & Holeman, E. (1985). A statistical model of auroral electron precipitation. Journal of Geophysical Research, 90(A5), 4229. https://doi.org/10.1029/JA090iA05p04229

Hardy, D. A., Gussenhoven, M. S., Raistrick, R., & McNeil, W. J. (1987). Statistical and functional representations of the pattern of auroral energy flux, number flux, and conductivity. Journal of Geophysical Research, 92(A11), 12275. https://doi.org/10.1029/JA092iA11p12275

Harel, M., Wolf, R. A., Reiff, P. H., Spiro, R. W., Burke, W. J., Rich, F. J., & Smiddy, M. (1981). Quantitative simulation of a magnetospheric substorm 1. Model logic and overview. Journal of Geophysical Research: Space Physics, 86(A4), 2217–2241. https://doi.org/10.1029/JA086iA04p02217

Hecht, J. H., Christensen, A. B., Strickland, D. J., Majeed, T., Gattinger, R. L., & Jones, A. V. (1999). A comparison between auroral particle characteristics and atmospheric composition inferred from analyzing optical emission measurements alone and in combination with incoherent scatter radar measurements. Journal of Geophysical Research: Space Physics, 104(A1), 33–44. https://doi.org/10.1029/1998JA900009

Hecht, J. H., Mulligan, T., Correira, J. T., Clemmons, J. H., Strickland, D. J., Walterscheid, R. L., & Conde, M. G. (2012). A multiyear (2002-2006) climatology of O/N $_2$ in the lower thermosphere from TIMED GUVI and ground-based photometer observations: O/N $_2$ IN THE LOWER THERMOSPHERE. Journal of Geophysical Research: Space Physics, 117(A3), n/a-n/a. https://doi.org/10.1029/2011JA017146

Hecht, J. H., Mulligan, T., Strickland, D. J., Kochenash, A. J., Murayama, Y., Tanaka, Y.-M., Evans, D. S., Conde, M. G., Donovan, E. F., Rich, F. J., & Morrison, D. (2008). Satellite and ground-based observations of auroral energy deposition and the effects on thermospheric composition during large geomagnetic storms: 1. Great geomagnetic storm of 20 November 2003. Journal of Geophysical Research: Space Physics, 113(A1). https://doi.org/10.1029/2007JA012365

Hedin, A. E. (1991). Extension of the MSIS Thermosphere Model into the middle and lower atmosphere. Journal of Geophysical Research: Space Physics, 96(A2), 1159–1172. https://doi.org/10.1029/90JA02125

Heinselman, C. J., & Nicolls, M. J. (2008). A Bayesian approach to electric field and E -region neutral wind estimation with the poker flat advanced modular incoherent scatter radar. *Radio Science*, **43**(5), RS5013. **https://doi.org/10.1029/2007RS003805**

Kaeppler, S. R., Markowski, D. G., Pepper, A. M., Troyer, R., Jaynes, A. N., Varney, R. H., & Hampton, D. (2023). Data-driven empirical conductance relations during auroral precipitation using incoherent scatter radar and all sky imagers. Journal of Geophysical Research: Space Physics, 128(9), e2023JA031764. https://doi.org/10.1029/2023JA031764

Keesee, A. M., Chen, M. W., Scime, E. E., & Lui, A. T. Y. (2014). Regions of ion energization observed during the Galaxy-15 substorm with TWINS: TWINS Galaxy-15. Journal of Geophysical Research: Space Physics, 119(10), 8274–8287. https://doi.org/10.1002/2014JA020466

Khazanov, G. V., & Chen, M. W. (2021). Why Atmospheric Backscatter Is Important in the Formation of Electron Precipitation in the Diffuse Aurora. Journal of Geophysical Research: Space Physics, 126(5), e2021JA029211. https://doi.org/10.1029/2021JA029211

Khazanov, G. V., Chen, M. W., Lemon, C. L., & Sibeck, D. G. (2019). The Magnetosphere-Ionosphere Electron Precipitation Dynamics and Their Geospace Consequences During the 17 March 2013 Storm. Journal of Geophysical Research: Space Physics, 124(8), 6504–6523. https://doi.org/10.1029/2019JA026589

Khazanov, G. V., & Glocer, A. (2020). How Magnetically Conjugate Atmospheres and the Magnetosphere Participate in the Formation of Low-Energy Electron Precipitation in the

Region of Diffuse Aurora. Journal of Geophysical Research: Space Physics, 125(8), e2020JA028057.

Khazanov, G. V., Koen, M. A., Konikov, Yu. V., & Sidorov, I. M. (1984). Simulation of ionosphere-plasmasphere coupling taking into account ion inertia and temperature anisotropy. Planetary and Space Science, 32(5), 585–598. https://doi.org/10.1016/0032-0633(84)90108-9

Khazanov, G. V., Sibeck, D. G., & Zesta, E. (2017). Major pathways to electron distribution function formation in regions of diffuse aurora: Electron Distribution Function Formation. Journal of Geophysical Research: Space Physics, 122(4), 4251–4265. https://doi.org/10.1002/2017JA023956

Kosch, M. J., Hagfors, T., & Schlegel, K. (1998). Extrapolating EISCAT Pedersen conductances to other parts of the sky using ground-based TV auroral images. Annales Geophysicae, 16(5), 583–588. https://doi.org/10.1007/s00585-998-0583-y

Lemon, C. (2003). Computing magnetospheric force equilibria. Journal of Geophysical Research, 108(A6). https://doi.org/10.1029/2002JA009702

Lemon, C., Wolf, R. A., Hill, T. W., Sazykin, S., Spiro, R. W., Toffoletto, F. R., Birn, J., & Hesse, M. (2004). Magnetic storm ring current injection modeled with the Rice Convection Model and a self-consistent magnetic field: RING CURRENT INJECTION SIMULATION. Geophysical Research Letters, 31(21), n/a-n/a. https://doi.org/10.1029/2004GL020914

Lin, D., Wang, W., Merkin, V. G., Huang, C., Oppenheim, M., Sorathia, K., Pham, K., Michael, A., Bao, S., Wu, Q., Zhang, Y., Wiltberger, M., Toffoletto, F., Lyon, J., & Garretson, J. (2022). Origin of Dawnside Subauroral Polarization Streams During Major Geomagnetic Storms. AGU Advances, 3(4), e2022AV000708. https://doi.org/10.1029/2022AV000708

Liu, J., Wang, W., Qian, L., Pham, K., Liu, L., Li, Q., Li, S., & Liu, X. (2023). Impacts of Ionospheric Conductance on Magnetosphere-Ionosphere Coupling. Journal of Geophysical Research: Space Physics, 128(2), e2022JA030864. https://doi.org/10.1029/2022JA030864

Lu, G. (2013). A Synthetic View of the Magnetospheric-Ionospheric Current System Associated with Substorms. In Magnetospheric Current Systems (pp. 199–207). American Geophysical Union (AGU). https://doi.org/10.1029/GM118p0199

McComas, D. J., Bame, S. J., Barraclough, B. L., Donart, J. R., Elphic, R. C., Gosling, J. T., Moldwin, M. B., Moore, K. R., & Thomsen, M. F. (1993). Magnetospheric plasma analyzer: Initial three-spacecraft observations from geosynchronous orbit. Journal of Geophysical Research: Space Physics, 98(A8), 13453–13465. https://doi.org/10.1029/93JA00726

McGranaghan, R., Knipp, D. J., & Matsuo, T. (2016). High-latitude ionospheric conductivity variability in three dimensions: THREE-DIMENSIONAL IONOSPHERIC CONDUCTIVITIES. Geophysical Research Letters, 43(15), 7867–7877. https://doi.org/10.1002/2016GL070253

McGranaghan, R., Knipp, D. J., Matsuo, T., Godinez, H., Redmon, R. J., Solomon, S. C., & Morley, S. K. (2015). Modes of high-latitude auroral conductance variability derived from DMSP energetic electron precipitation observations: Empirical orthogonal function analysis. Journal of Geophysical Research: Space Physics, 120(12), 11,013-11,031. https://doi.org/10.1002/2015JA021828

Mende, S. B., Heetderks, H., Frey, H. U., Lampton, M., Geller, S. P., Habraken, S., Renotte, E., Jamar, C., Rochus, P., Spann, J., Fuselier, S. A., Gerard, J.-C., Gladstone, R., Murphree, S., &

Cogger, L. (2000). Far ultraviolet imaging from the IMAGE spacecraft. 1. System design. Space Science Reviews, 91(1–2), 243–270. https://doi.org/10.1023/A:1005271728567

Meng, X., Ozturk, D. S., Verkhoglyadova, O. P., Varney, R. H., Reimer, A. S., Semeter, J. L., Kaeppler, S. R., & Zhan, W. (2023). Energy deposition by mesoscale high-latitude electric fields into the thermosphere during the 26 October 2019 geomagnetic storm. Journal of Geophysical Research: Space Physics, https://doi/10.1029/2022JA030716.

Newell, P. T., Liou, K., Zhang, Y., Sotirelis, T., Paxton, L. J., & Mitchell, E. J. (2014). OVATION Prime-2013: Extension of auroral precipitation model to higher disturbance levels. Space Weather, 12(6), 368–379. https://doi.org/10.1002/2014SW001056

Newell, P. T., Sotirelis, T., & Wing, S. (2009). Diffuse, monoenergetic, and broadband aurora: The global precipitation budget: GLOBAL PRECIPITATION BUDGET. Journal of Geophysical Research: Space Physics, 114(A9), n/a-n/a. https://doi.org/10.1029/2009JA014326

Newell, P. T., Sotirelis, T., & Wing, S. (2010). Seasonal variations in diffuse, monoenergetic, and broadband aurora. Journal of Geophysical Research: Space Physics, 115(A3). https://doi.org/10.1029/2009JA014805

Ni, B., Thorne, R., Liang, J., Angelopoulos, V., Cully, C., Li, W., Zhang, X., Hartinger, M., Le Contel, O., & Roux, A. (2011). Global distribution of electrostatic electron cyclotron harmonic waves observed on THEMIS: GLOBAL DISTRIBUTION OF ECH WAVES. Geophysical Research Letters, 38(17), n/a-n/a. https://doi.org/10.1029/2011GL048793

Ni, B., Thorne, R. M., Meredith, N. P., Shprits, Y. Y., & Horne, R. B. (2011). Diffuse auroral scattering by whistler mode chorus waves: Dependence on wave normal angle distribution: AURORAL SCATTERING BY WHISTLER MODE CHORUS WAVES. Journal of Geophysical Research: Space Physics, 116(A10), n/a-n/a. https://doi.org/10.1029/2011JA016517

Orlova, K., & Shprits, Y. (2014). Model of lifetimes of the outer radiation belt electrons in a realistic magnetic field using realistic chorus wave parameters: Electron lifetimes in non-dipole field. Journal of Geophysical Research: Space Physics, 119(2), 770–780. https://doi.org/10.1002/2013JA019596

Orlova, K., Spasojevic, M., & Shprits, Y. (2014). Activity-dependent global model of electron loss inside the plasmasphere: ELECTRON LIFETIMES DUE TO HISS. Geophysical Research Letters, 41(11), 3744–3751. https://doi.org/10.1002/2014GL060100

Paxton, L. J., Christensen, A. B., Humm, D. C., Ogorzalek, B. S., Pardoe, C. T., Morrison, D., Weiss, M. B., Crain, W., Lew, P. H., Mabry, D. J., Goldsten, J. O., Gary, S. A., Persons, D. F., Harold, M. J., Alvarez, E. B., Ercol, C. J., Strickland, D. J., & Meng, C.-I. (1999). Global ultraviolet imager (GUVI): Measuring composition and energy inputs for the NASA Thermosphere Ionosphere Mesosphere Energetics and Dynamics (TIMED) mission. Optical Spectroscopic Techniques and Instrumentation for Atmospheric and Space Research III, 3756, 265–276. https://doi.org/10.1117/12.366380

Perlongo, N. J., Ridley, A. J., Liemohn, M. W., & Katus, R. M. (2017). The effect of ring current electron scattering rates on magnetosphere-ionosphere coupling. Journal of Geophysical Research: Space Physics, 122(4), 4168–4189. https://doi.org/10.1002/2016JA023679

Picone, J. M., Hedin, A. E., Drob, D. P., & Aikin, A. C. (2002). NRLMSISE-00 empirical model of the atmosphere: Statistical comparisons and scientific issues: TECHNIQUES. Journal of

Geophysical Research: Space Physics, 107(A12), SIA 15-1-SIA 15-16. https://doi.org/10.1029/2002JA009430
Raeder, J., Wang, Y., & Fuller-Rowell, T. J. (2013). Geomagnetic Storm Simulation with a Coupled Magnetosphere-Ionosphere-Thermosphere Model. In P. Song, H. J. Singer, & G. L. Siscoe (Eds.), Geophysical Monograph Series (pp. 377–384). American Geophysical Union. https://doi.org/10.1029/GM125p0377
Richmond, A. D., & Kamide, Y. (1988). Mapping electrodynamic features of the high-latitude ionosphere from localized observations: Technique. Journal of Geophysical Research: Space Physics, 93(A6), 5741–5759. https://doi.org/10.1029/JA093iA06p05741
Rideout W., Cariglia K. CEDAR Madrigal Database URL: http://cedar.openmadrigal.org
Ridley, A. J., De Zeeuw, D. L., Gombosi, T. I., & Powell, K. G. (2001). Using steady state MHD results to predict the global state of the magnetosphere-ionosphere system. Journal of Geophysical Research: Space Physics, 106(A12), 30067–30076. https://doi.org/10.1029/2000JA002233
Robinson, R. M., Kaeppler, S. R., Zanetti, L., Anderson, B., Vines, S. K., Korth, H., & Fitzmaurice, A. (2020). Statistical Relations Between Auroral Electrical Conductances and Field-Aligned Currents at High Latitudes. Journal of Geophysical Research: Space Physics, 125(7), e2020JA028008. https://doi.org/10.1029/2020JA028008
Robinson, R. M., Vondrak, R. R., Miller, K., Dabbs, T., & Hardy, D. (1987). On calculating ionospheric conductances from the flux and energy of precipitating electrons. Journal of Geophysical Research, 92(A3), 2565. https://doi.org/10.1029/JA092iA03p02565
Sazykin, S., Spiro, R. W., Wolf, R. A., Toffoletto, F. R., Tsyganenko, N., Goldstein, J., & Hairston, M. R. (2005). Modeling inner magnetospheric electric fields: Latest self-consistent results. In

T. I. Pulkkinen, N. A. Tsyganenko, & R. H. W. Friedel (Eds.), Geophysical Monograph Series (Vol. 155, pp. 263–269). American Geophysical Union. https://doi.org/10.1029/155GM28

Shprits, Y. Y., Li, W., & Thorne, R. M. (2006). Controlling effect of the pitch angle scattering rates near the edge of the loss cone on electron lifetimes. Journal of Geophysical Research: Space Physics, 111(A12). https://doi.org/10.1029/2006JA011758

Solomon, S. C. (1993). Auroral electron transport using the Monte Carlo Method. Geophysical Research Letters, 20(3), 185–188. https://doi.org/10.1029/93GL00081

Solomon, S. C. (2001). Auroral particle transport using Monte Carlo and hybrid methods. Journal of Geophysical Research: Space Physics, 106(A1), 107–116. https://doi.org/10.1029/2000JA002011

Solomon, S. C., Hays, P. B., & Abreu, V. J. (1988). The auroral 6300 Å emission: Observations and modeling. Journal of Geophysical Research: Space Physics, 93(A9), 9867–9882. https://doi.org/10.1029/JA093iA09p09867

Strickland, D. J., Daniell, R. E., Jasperse, J. R., & Basu, B. (1993). Transport-Theoretic Model for the Electron-Proton-Hydrogen Atom Aurora, 2. Model Results. Journal of Geophysical Research, 98(A12), 21533–21548. https://doi.org/10.1029/93JA01645

Thorne, R. M. (2010). Radiation belt dynamics: The importance of wave-particle interactions: FRONTIER. Geophysical Research Letters, 37(22), n/a-n/a. https://doi.org/10.1029/2010GL044990

Toffoletto, F. (2020). Chapter 4—Modeling techniques. In V. K. Jordanova, R. Ilie, & M. W. Chen (Eds.), Ring Current Investigations (pp. 99–151). Elsevier. https://doi.org/10.1016/B978-0-12-815571-4.00004-4

Toffoletto, F., Sazykin, S., Spiro, R., & Wolf, R. (2003). Inner Magnetospheric Modeling with the Rice Convection Model. In A. C.-L. Chian, I. H. Cairns, S. B. Gabriel, J. P. Goedbloed, T. Hada, M. Leubner, L. Nocera, R. Stening, F. Toffoletto, C. Uberoi, J. A. Valdivia, U. Villante, C.-C. Wu, & Y. Yan (Eds.), Advances in Space Environment Research—Volume I (pp. 175–196). Springer Netherlands. https://doi.org/10.1007/978-94-007-1069-6_19

Torr, M. R., Torr, D. G., Zukic, M., Johnson, R. B., Ajello, J., Banks, P., Clark, K., Cole, K., Keffer, C., Parks, G., Tsurutani, B., & Spann, J. (1995). A far ultraviolet imager for the

International Solar-Terrestrial Physics Mission. Space Science Reviews, 71(1–4), 329–383. https://doi.org/10.1007/BF00751335

Tsyganenko, N. A., & Mukai, T. (2003). Tail plasma sheet models derived from Geotail particle data. Journal of Geophysical Research: Space Physics, 108(A3). https://doi.org/10.1029/2002JA009707

Tsyganenko, N. A., & Sitnov, M. I. (2005). Modeling the dynamics of the inner magnetosphere during strong geomagnetic storms. Journal of Geophysical Research: Space Physics, 110(A3). https://doi.org/10.1029/2004JA010798

Valentic, T., *et al*., "AMISR the advanced modular incoherent scatter radar," *2013 IEEE International Symposium on Phased Array Systems and Technology*, Waltham, MA, USA, 2013, pp. 659-663, doi: 10.1109/ARRAY.2013.6731908.

Wallis, D. D., & Budzinski, E. E. (1981). Empirical models of height integrated conductivities. Journal of Geophysical Research: Space Physics, 86(A1), 125–137. https://doi.org/10.1029/JA086iA01p00125

Wang, Z., & Zou, S. (2022). COMPASS: A New COnductance Model Based on PFISR And SWARM Satellite Observations. Space Weather, 20(2), e2021SW002958. https://doi.org/10.1029/2021SW002958

Weimer, D. R. (2001). An improved model of ionospheric electric potentials including substorm perturbations and application to the Geospace Environment Modeling November 24, 1996, event. Journal of Geophysical Research: Space Physics, 106(A1), 407–416. https://doi.org/10.1029/2000JA000604

Wiltberger, M., Wang, W., Burns, A. G., Solomon, S. C., Lyon, J. G., & Goodrich, C. C. (2004). Initial results from the coupled magnetosphere ionosphere thermosphere model: Magnetospheric and ionospheric responses. Journal of Atmospheric and Solar-Terrestrial Physics, 66(15), 1411–1423. https://doi.org/10.1016/j.jastp.2004.03.026

Wing, S., Khazanov, G. V., Sibeck, D. G., & Zesta, E. (2019). Low Energy Precipitating Electrons in the Diffuse Aurorae. Geophysical Research Letters, 46(7), 3582–3589. https://doi.org/10.1029/2019GL082383

Young, D. T., Balsiger, H., & Geiss, J. (1982). Correlations of magnetospheric ion composition with geomagnetic and solar activity. Journal of Geophysical Research, 87(A11), 9077. https://doi.org/10.1029/JA087iA11p09077

Yu, Y., Jordanova, V. K., McGranaghan, R. M., & Solomon, S. C. (2018). Self-Consistent Modeling of Electron Precipitation and Responses in the Ionosphere: Application to Low-Altitude Energization During Substorms. Geophysical Research Letters, 45(13), 6371–6381. https://doi.org/10.1029/2018GL078828

Zhang, Y., & Paxton, L. J. (2008). An empirical Kp-dependent global auroral model based on TIMED/GUVI FUV data. Journal of Atmospheric and Solar-Terrestrial Physics, 70(8), 1231–1242. https://doi.org/10.1016/j.jastp.2008.03.008

Zhang, S.-R., Erickson, P. J., Zhang, Y., Wang, W., Huang, C., Coster, A. J., et al. (2017). Observations of ion-neutral coupling associated with strong electrodynamic disturbances during the 2015 St. Patrick's Day storm. *Journal of Geophysical Research: Space Physics*, *122*(1), 1314–1337, doi:10.1002/2016ja023307.

Zheng, Y., Brandt, P. C., Lui, A. T. Y., & Fok, M.-C. (2008). On ionospheric trough conductance and subauroral polarization streams: Simulation results. Journal of Geophysical Research: Space Physics, 113(A4). https://doi.org/10.1029/2007JA012532

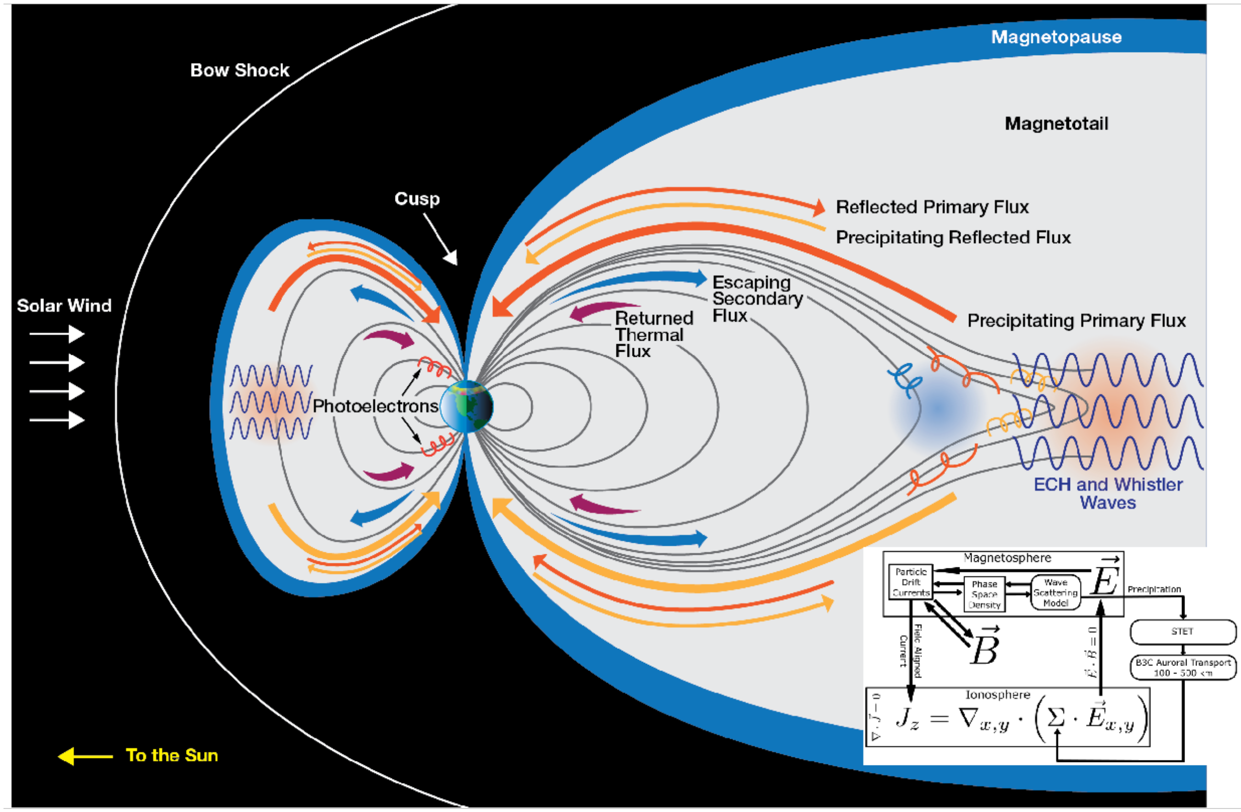

Figure 1. Schematic illustration of magnetosphere-ionosphere coupling of precipitating electron flux in STET and the RCM-E models. The cartoon is a meridional view of the Earth's magnetosphere where the black lines are representative field lines. The flow chart illustrates the electrodynamic coupling in the RCM-E.

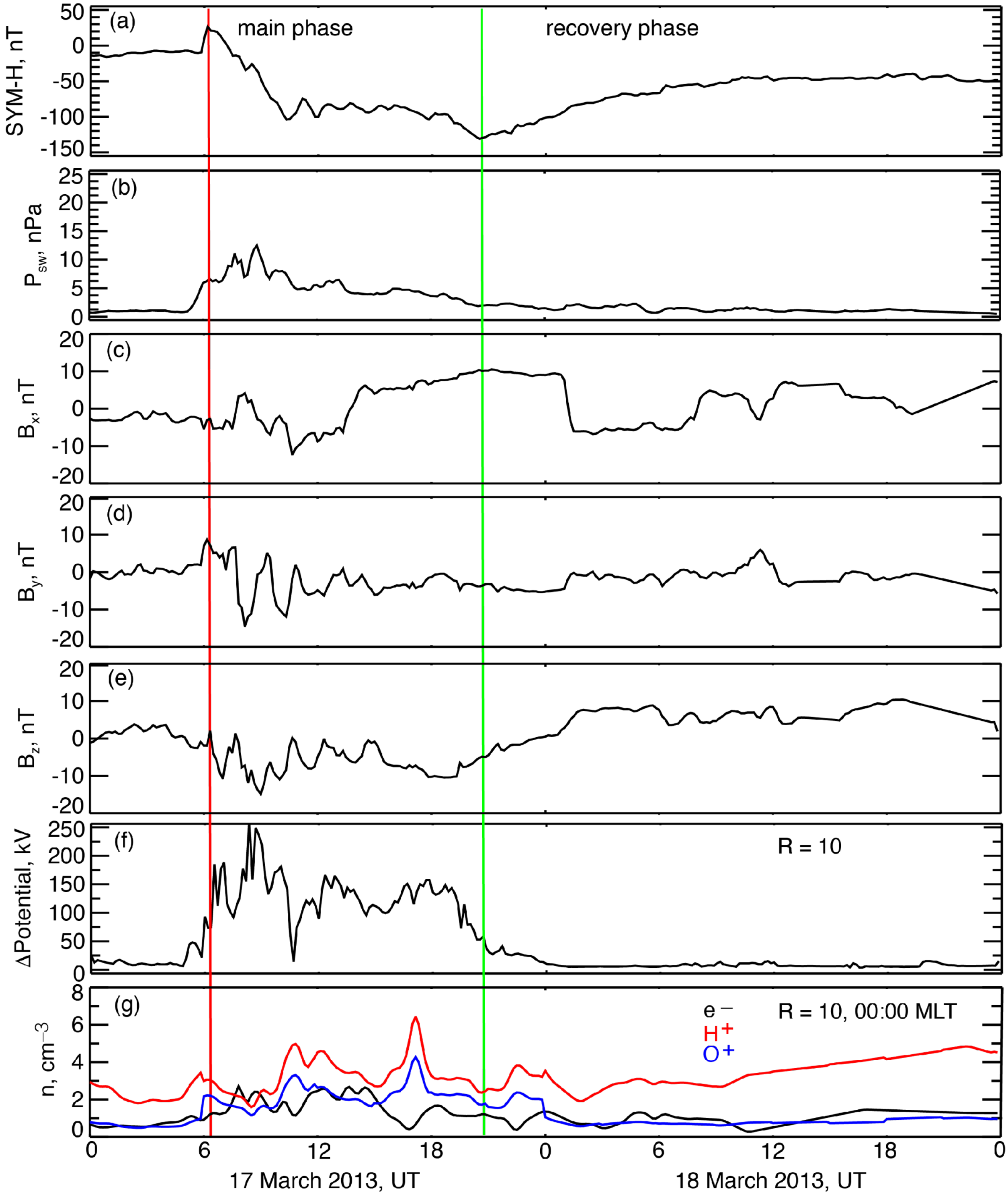

Figure 2. The geomagnetic and solar wind indices, and representative RCM-E boundary conditions for the 17–18 March 2013 storm. Time traces of (a) SYM-H, (b) dynamic solar wind pressure, and (c, d, e) the x, y, and z components of IMF. At 10 R_E and 00:00 MLT or midnight, time traces of the RCM-E (f) electric potential and (g) electron (black), H^+ (red) and O^+ (blue) density (not including the plasmasphere density component).

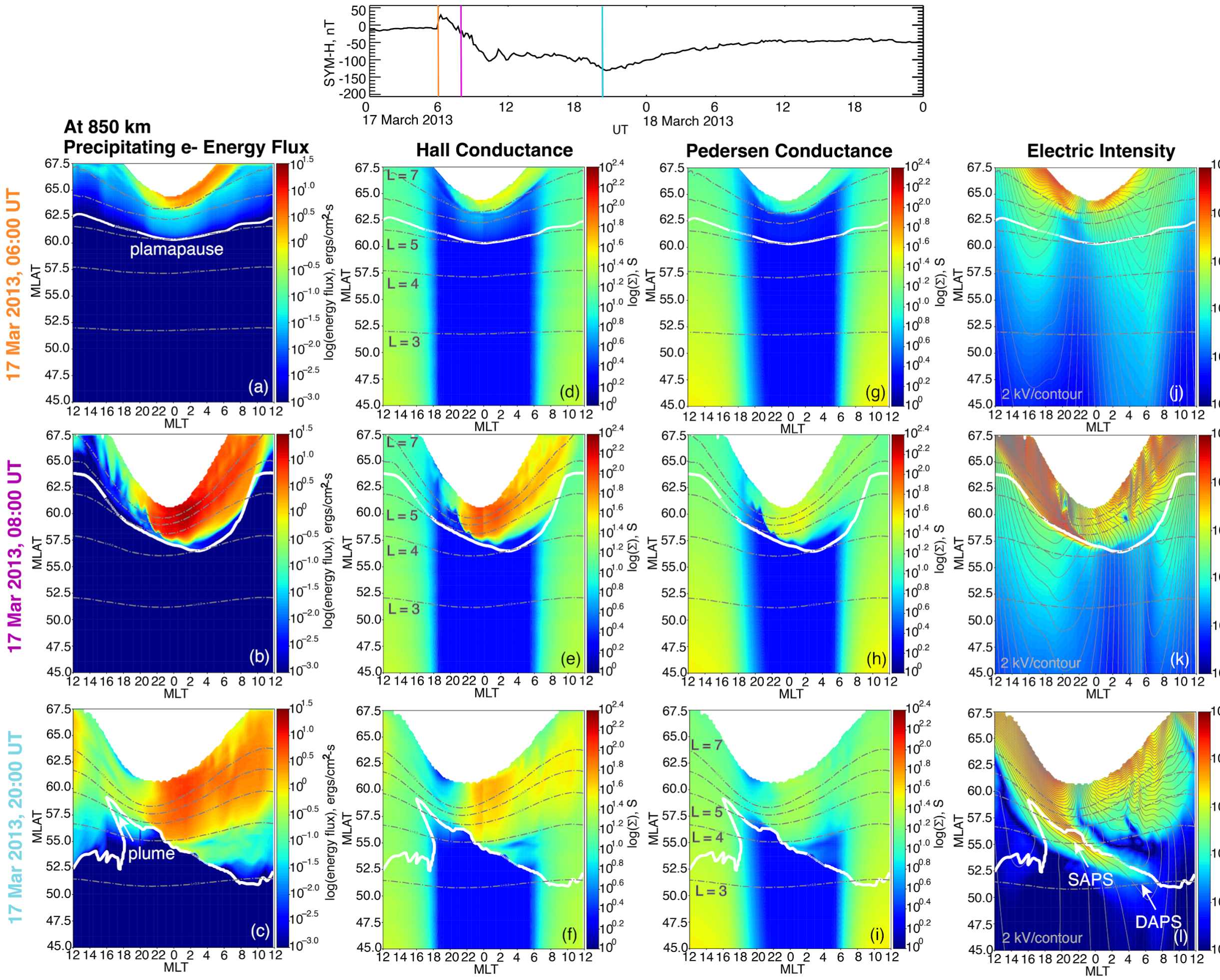

Figure 3. Simulated (a-c) precipitating electron energy flux, (d-f) Hall conductance, (g-i) Pedersen conductance, and (j-l) electric intensity for 17 March 2013 at 06:00 UT (pre-storm), 08:00 UT (early main phase), and 20:00 UT (late main phase) at 850 km in the ionosphere. The solid white curve depicts the model plasmapause and the dashed gray curves are representative *L* shells. The solid gray curves in (j, k, l) are equipotential contours spaced every 2 kV per contour. The top panel shows a time trace of SYM-H for March 17–18, 2013.

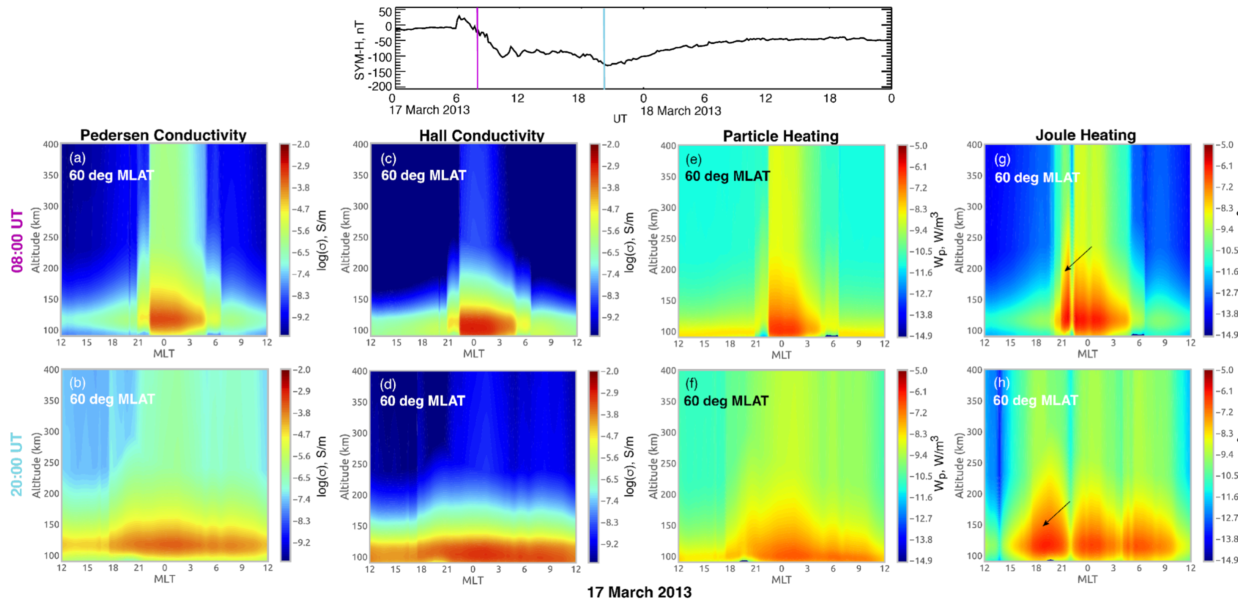

Figure 4. Simulated altitudinal profiles of (a, b) Pedersen conductivity, (c, d) Hall conductivity, (e, f) particle heating, and (g, h) joule heating at 60° MLAT for 08:00 UT and 20:00 UT on March 17, 2013. The top panel shows a time trace of SYM-H for March 17–18, 2013.

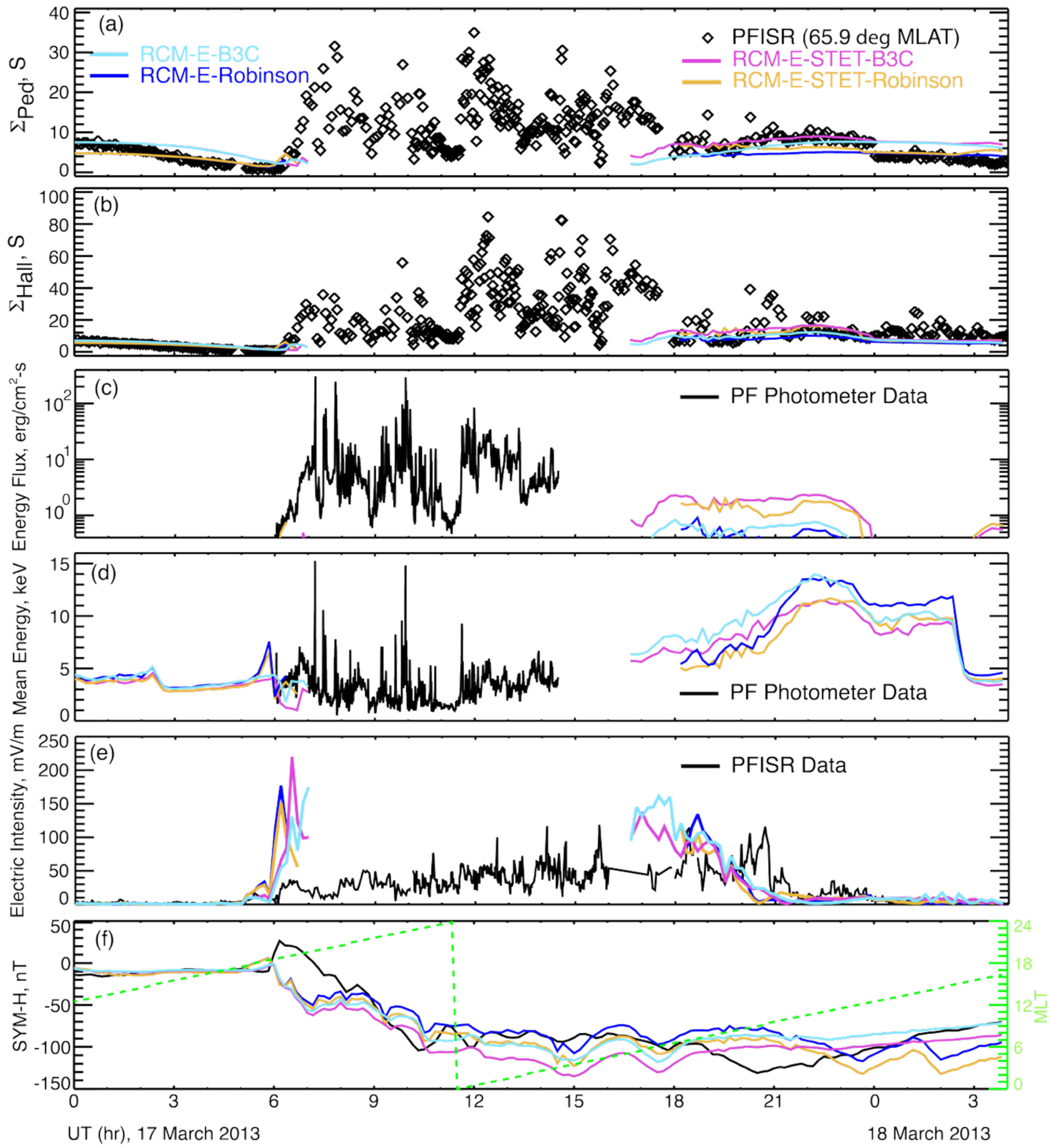

Figure 5. Comparisons of simulation results with Poker Flat observations for 17-18 March 2013. The (a) Pedersen and (b) Hall conductance inferred from PFISR measurements are shown as black diamonds. The Pedersen and Hall conductance with four different model runs are shown: RCM-E-STET-B3C (pink), RCM-E-B3C (cyan), RCM-E-Robinson (blue), RCM-E-STET-Robinson (gold). The (c) electron energy flux and (d) mean electron energy measured by the Poker Flat photometer. Model results with the RCM-E-STET-B3C (pink) and RCM-E-B3C (cyan) are also shown. (e) The PFISR electric intensity. The RCM-E-STET-B3C (pink) and RCM-E-B3C (cyan) results are shown for comparison. (f) The SYM-H (black curve) and simulated SYM-H are shown. The simulated SYM-H are calculated using a pressure-corrected Dessler-Parker-Sckopke relation given by eq. (6) in Chen et al. (2019). The green dashed curve shows the MLT of Poker Flat Research Range.

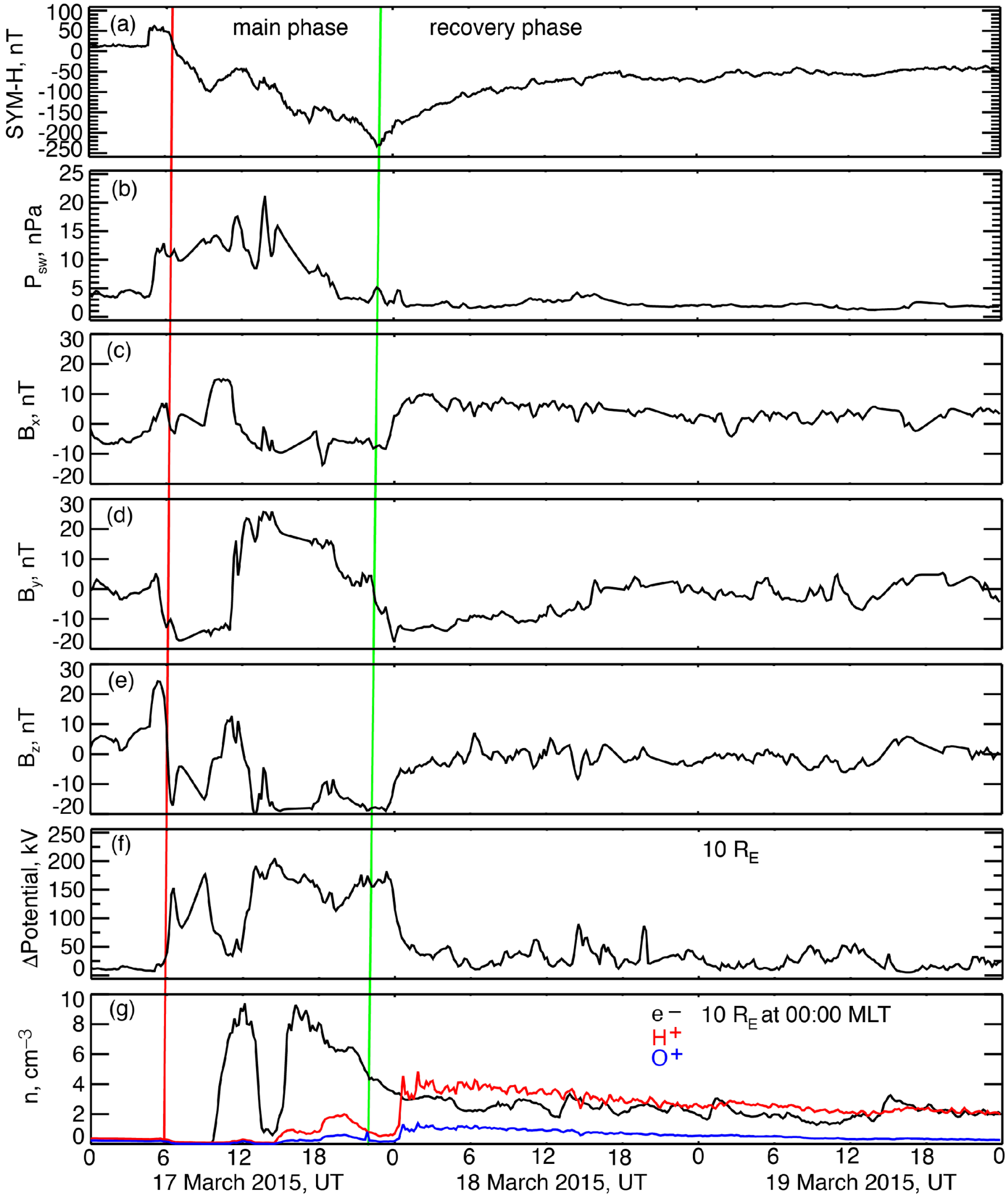

Figure 6. The geomagnetic and solar wind indices, and representative RCM-E boundary conditions for the 17–19 March 2015 storm. Time traces of (a) SYM-H, (b) dynamic solar wind pressure, and the (c, d, e) x, y, and z components of IMF. At 10 R_E time traces of the RCM-E (f) electric potential and at 00:00 MLT the (g) electron (black), H^+ (red) and O^+ (blue) density (not including the plasmasphere density component).

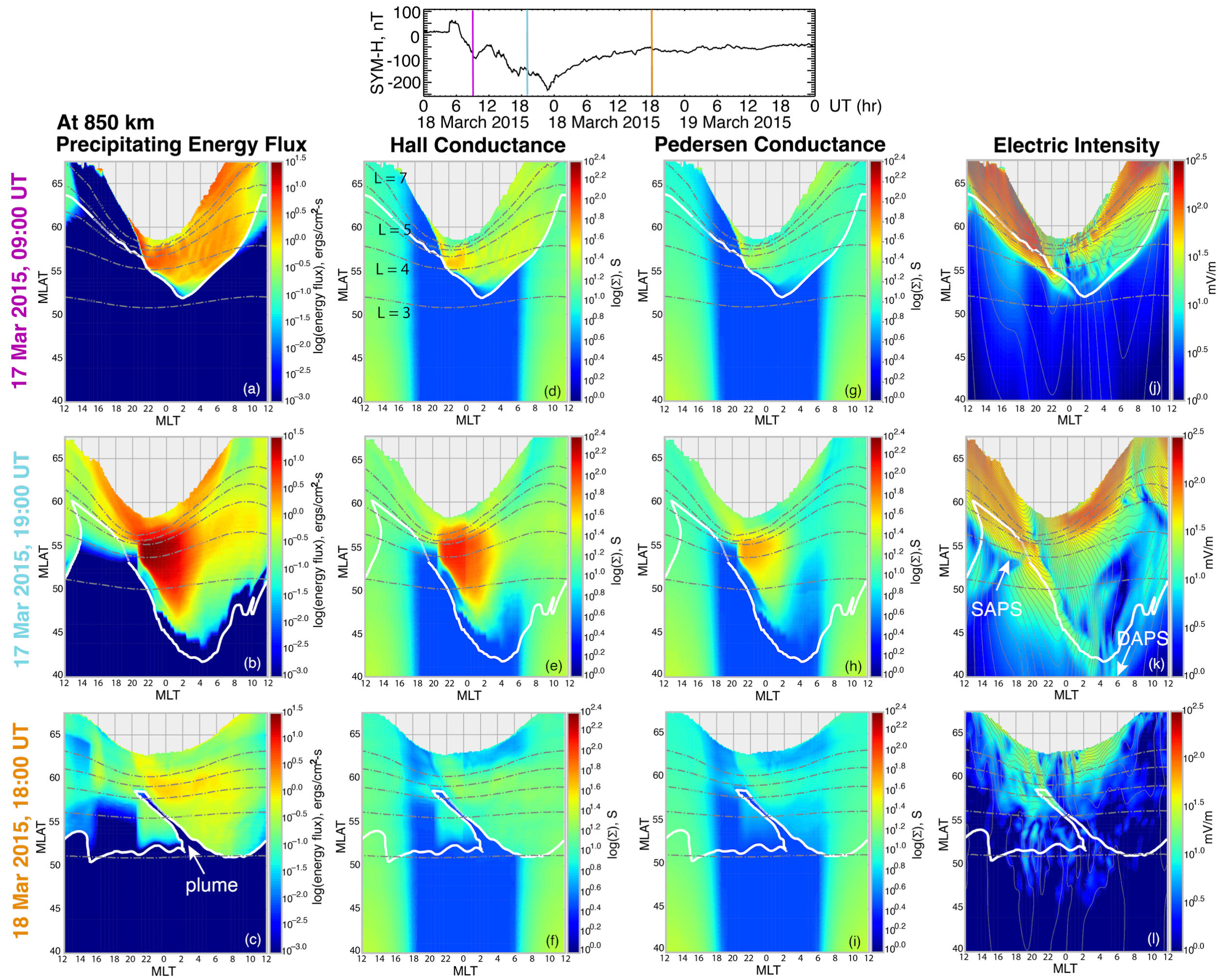

Figure 7. Simulated (a-c) precipitating electron energy flux, (d-f) Hall conductance, (g-i) Pedersen conductance, and (j-l) electric intensity for 17 March 2015 at 09:00 UT (early main phase), 19:00 UT (late main phase), and 18 March 2015 at 18:00 UT (recovery phase) at 850 km in the ionosphere. The solid white curve shows the model plasmapause and the dashed gray curves are representative *L* shells. The solid gray curves in (j, k, l) are equipotential contours spaced every 2 kV per contour. The top panel shows SYM-H for 17–18 March 2013.

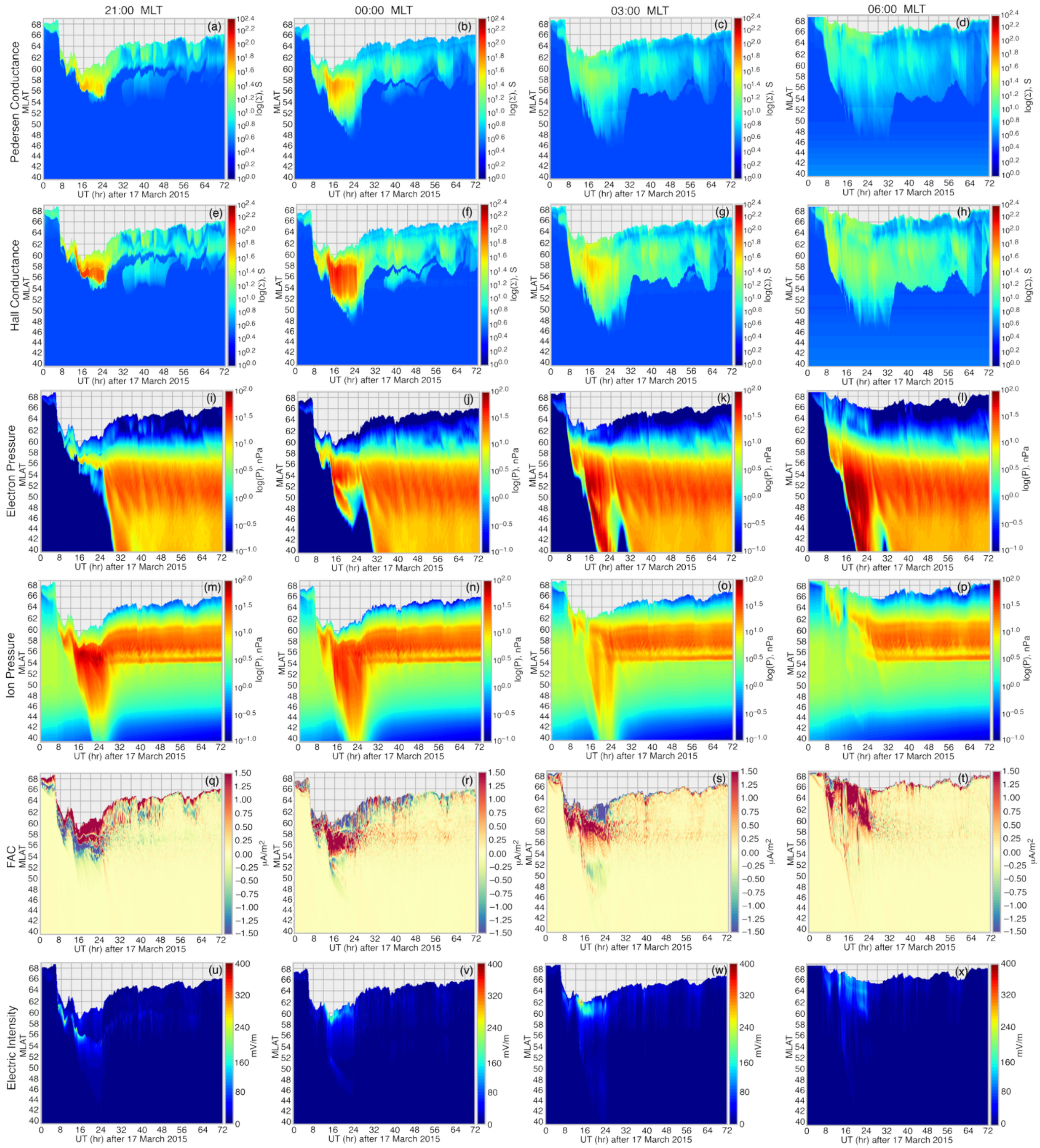

Figure 8. MLAT versus UT maps of the simulated (a, b, c, d) Pedersen conductance, (d, e, f, g) Hall conductance, (i, j, k, l) electron pressure, (m, n, o, p) ion pressure, (q, r, s, t) field-aligned currents (FAC) (u, v, w, x) electric intensity at fixed 21:00 MLT, 0:00 MLT, and 03:00 MLT, respectively. The simulated quantities that are mapped to the ionosphere at 850 km. Blue/red corresponds to field-aligned currents flowing into/out of the ionosphere.

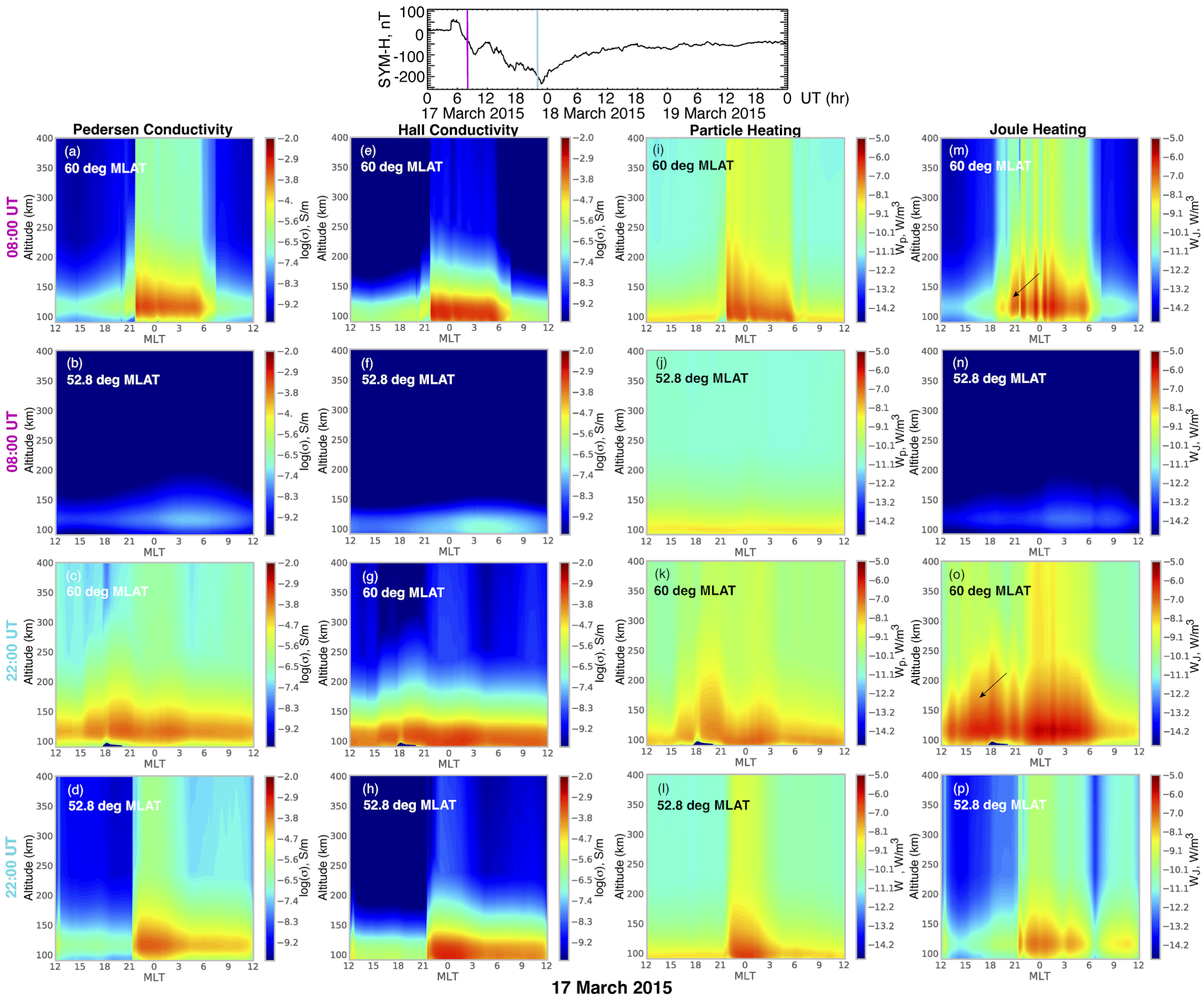

Figure 9. Altitude-MLT maps at 08:00 UT (early main phase) and 22:00 UT (late main phase) and at 60° MLAT and 52.5° MLAT of simulated of Pedersen conductivity, Hall conductivity, particle heating, and joule heating.

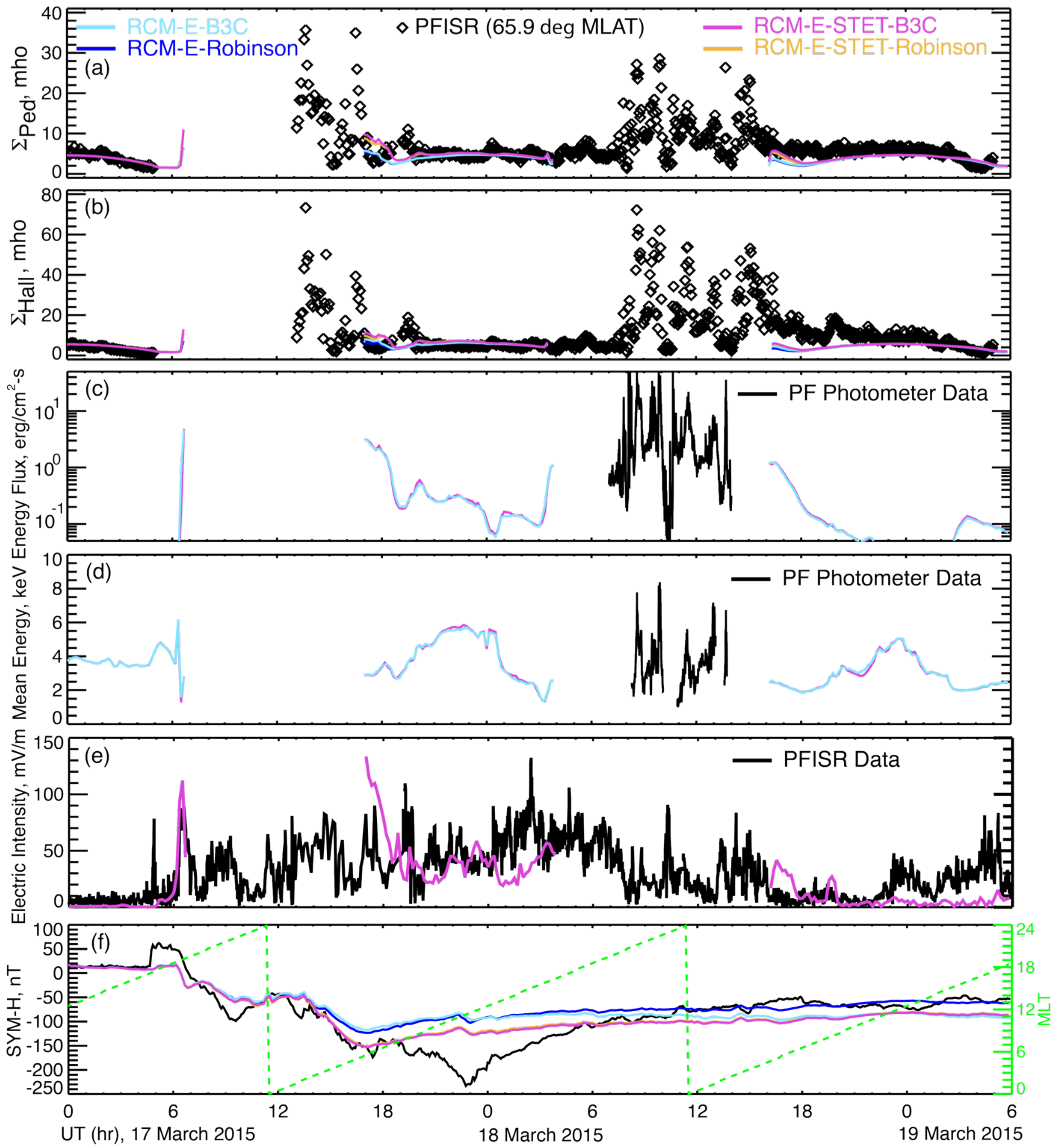

Figure 10. Comparisons of simulation results with Poker Flat observations for 17-18 March 2015. The (a) Pedersen and (b) Hall conductance inferred from PFISR measurements are shown as black diamonds. The RCM-E-STET-B3C (pink) conductance are overplotted. The (c) electron energy flux and (d) mean electron energy measured by the Poker Flat photometer. Model results (pink) are also shown. (e) The PFISR electric intensity. The RCM-E-STET-B3C (pink) are overplotted. (f) The SYM-H (black curve) and simulated SYM-H are shown. The green dashed curve shows the MLT of the Poker Flat Research Range.

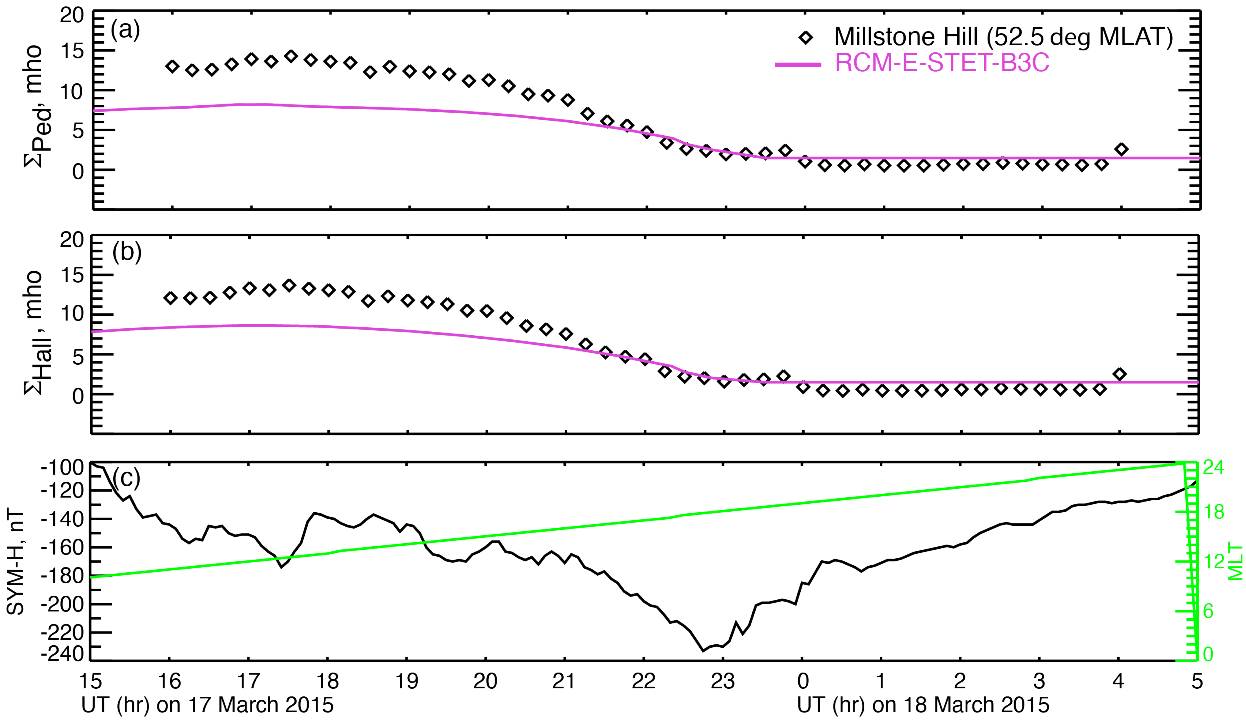

Figure 11. Comparisons of the Millstone Hill ISR (black diamonds) and simulated (pink curve) (a) Pedersen and (b) Hall conductance at 52.5° MLAT. (c) SYM-H over 17 March 2015 at 15:00 UT to 18 March 2015 at 05:00 UT. The green curve is the MLT of Millstone Hill Geospace Facility.